



# 1      **Energy-conservation datasets of global land surface radiation** 2      **and heat fluxes from 2000-2020 generated by CoSEB**

3      Junrui Wang<sup>a, b</sup>, Ronglin Tang<sup>a, b, \*</sup>, Meng Liu<sup>c</sup>, Zhao-Liang Li<sup>a, b, c</sup>

4      <sup>a</sup> State Key Laboratory of Resources and Environment Information System, Institute of  
 5      Geographic Sciences and Natural Resources Research, Chinese Academy of Sciences,  
 6      Beijing 100101, China

7      <sup>b</sup> University of Chinese Academy of Sciences, Beijing 100049, China

8      <sup>c</sup> State Key Laboratory of Efficient Utilization of Arable Land in China, Institute of  
 9      Agricultural Resources and Regional Planning, Chinese Academy of Agricultural  
 10      Sciences, Beijing 100081, China

11      \* Authors to whom correspondence should be addressed: tangrl@lreis.ac.cn

## 12      **Abstract**

13      Accurately estimating global land surface radiation [including downward  
 14      shortwave radiation ( $SW_{IN}$ ), downward longwave radiation ( $LW_{IN}$ ), upward shortwave  
 15      radiation ( $SW_{OUT}$ ), upward longwave radiation ( $LW_{OUT}$ ) and net radiation (Rn)] and heat  
 16      fluxes [including latent heat flux (LE), soil heat flux (G) and sensible heat flux (H)] is  
 17      essential for quantifying the exchange of radiation, heat and water between the land and  
 18      atmosphere under global climate change. This study presents the first energy-  
 19      conservation datasets of global land surface radiation and heat fluxes from 2000 to 2020,  
 20      generated by our model of Coordinated estimates of land Surface Energy Balance  
 21      components (CoSEB) that was renewed with a combination of GLASS and MODIS  
 22      remote sensing data, ERA5-Land reanalysis datasets, topographic data, CO<sub>2</sub>  
 23      concentration data, and observations at 258 eddy covariance sites worldwide from the  
 24      AmeriFlux, FLUXNET, EuroFlux, OzFlux, ChinaFLUX and TPDC. The developed  
 25      CoSEB-based datasets are strikingly advantageous in that [1] they are the first RS-based  
 26      global datasets that satisfy both surface radiation balance ( $SW_{IN} - SW_{OUT} + LW_{IN} -$   
 27       $LW_{OUT} = Rn$ ) and heat balance ( $LE + H + G = Rn$ ) among the eight fluxes, as



demonstrated by both the radiation imbalance ratio [RIR, defined as  $100\% \times (SW_{IN} - SW_{OUT} + LW_{IN} - LW_{OUT})/R_n$ ] and energy imbalance ratio [EIR, defined as  $100\% \times (R_n - G - LE - H)/R_n$ ] of 0, [2] the radiation and heat fluxes are characterized by high accuracies, where (1) the RMSEs for daily estimates of  $SW_{IN}$ ,  $SW_{OUT}$ ,  $LW_{IN}$ ,  $LW_{OUT}$ ,  $R_n$ ,  $LE$ ,  $H$  and  $G$  from the CoSEB-based datasets were 28.51 W/m<sup>2</sup>, 10.39 W/m<sup>2</sup>, 14.29 W/m<sup>2</sup>, 10.62 W/m<sup>2</sup>, 22.40 W/m<sup>2</sup>, 24.38 W/m<sup>2</sup>, 22.67 W/m<sup>2</sup> and 6.77 W/m<sup>2</sup>, respectively, as well as for 8-day estimates were 12.81 W/m<sup>2</sup>, 7.08 W/m<sup>2</sup>, 9.22 W/m<sup>2</sup>, 8.34 W/m<sup>2</sup>, 13.38 W/m<sup>2</sup>, 19.99 W/m<sup>2</sup>, 17.44 W/m<sup>2</sup> and 4.25 W/m<sup>2</sup>, respectively, (2) the CoSEB-based datasets, in comparison to the mainstream products/datasets (i.e. GLASS, BESS-Rad, BESSV2.0, FLUXCOM, MOD16A2, PML\_V2 and ETMonitor) that generally separately estimated subsets of the eight flux components, better agreed with the in situ observations. Our developed datasets hold significant potential for application across diverse fields such as agriculture, forestry, hydrology, meteorology, ecology, and environmental science, which can facilitate comprehensive studies on the variability, impacts, responses, adaptation strategies, and mitigation measures of global and regional land surface radiation and heat fluxes under the influences of climate change and human activities. The CoSEB-based datasets are open access and available through the National Tibetan Plateau Data Center (TPDC) at <https://doi.org/10.11888/Terre.tpdc.302559> (Tang et al., 2025a) and through the Science Data Bank (ScienceDB) at <https://doi.org/10.57760/sciencedb.27228> (Tang et al., 2025b).

**Key words:** Surface energy balance; Surface radiation balance; Shortwave/Longwave radiation; Net radiation; Sensible/Latent heat flux; Evapotranspiration; CoSEB

## 1 Introduction

Land surface radiation balance and heat balance play important roles in Earth's climate system, representing the physical processes by which the surface-atmosphere absorbs and redistributes radiation and heat fluxes (Berbery et al., 1999; Betts et al., 1996; Mueller et al., 2009; Sellers et al., 1997; Xu et al., 2022a), and facilitating the



56 exchange of water, energy, carbon, and other agents essential to climatic and ecological  
 57 systems and human society (Jia et al., 2013; Wang et al., 2012; Wild, 2009; Wild et al.,  
 58 2012; Xia et al., 2006). Accurately monitoring the spatial and temporal variations of  
 59 global land surface radiation [including downward shortwave radiation ( $SW_{IN}$ ),  
 60 downward longwave radiation ( $LW_{IN}$ ), upward shortwave radiation ( $SW_{OUT}$ ), upward  
 61 longwave radiation ( $LW_{OUT}$ ) and net radiation ( $R_n$ )] and heat fluxes [including latent  
 62 heat flux ( $LE$ ), soil heat flux ( $G$ ) and sensible heat flux ( $H$ )] is indispensable for  
 63 quantifying the exchange of radiation, heat and water between the land and atmosphere  
 64 under global climate change (Ersi et al., 2024; Liang et al., 2019; Rios & Ramamurthy,  
 65 2022; Tang et al., 2024a; Wang et al., 2021), and for studying solar energy utilization  
 66 (Tang et al., 2024b; Zhang et al., 2017), hydrological cycle (Huang et al., 2015; Wild &  
 67 Liepert, 2010), ecosystem productivity (Nemani et al., 2003), agricultural management  
 68 (De Wit et al., 2005) and ecological protection (Tang et al., 2023). Remote sensing (RS)  
 69 technology, with its high spatial-temporal resolution and applicability over large areas,  
 70 is considered to be the most effective and economical means for obtaining global land  
 71 surface radiation and heat fluxes (Liu et al., 2016; Van Der Tol, 2012; Zhang et al.,  
 72 2010).

73 In past decades, numerous RS-based products/datasets of global surface radiation  
 74 and heat fluxes have significantly advanced, which were generally generated by  
 75 physical or statistical methods (Jiao et al., 2023; Jung et al., 2019; Martens et al., 2017;  
 76 Yu et al., 2022). However, two key limitations still exist in these products. Firstly, most  
 77 available products provide only a single component of land surface radiation or heat  
 78 fluxes, e.g. ETMonitor (Zheng et al., 2022) and MOD16A2 (Mu et al., 2011) only  
 79 estimating  $LE$ , leading to the failure to satisfy surface radiation balance and heat  
 80 balance when the single radiation or heat flux is utilized in conjunction with products  
 81 containing other radiation and heat components (Wang et al., 2025), and further posing  
 82 significant uncertainties to understand the interactions and redistributions of surface  
 83 radiation and energy in the Earth-atmosphere system. Secondly, a few products, e.g.



84 FLUXCOM (Jung et al., 2019) and GLASS (Jiang et al., 2015; Zhang et al., 2014),  
85 generated datasets for multiple components of surface radiation and heat fluxes by using  
86 independent estimates from the uncoordinated models, which make them difficult to  
87 abide by surface radiation and heat conservation. These energy-imbalanced and  
88 radiation-imbalanced estimates among multiple components from previous  
89 products/datasets severely limit their in-depth applications in analyzing the spatial and  
90 temporal trends, simulating the physical process of radiation, heat and water cycles as  
91 well as revealing the attributions and mechanisms in Earth-surface system under global  
92 climate change. It was impending and imperative to develop global datasets of land  
93 surface radiation and heat fluxes characterized by high accuracies, radiation balance as  
94 well as heat balance, to better meet the requirements in practical applications of various  
95 fields.

96 Our proposed data-driven model/framework of Coordinated estimates of land  
97 Surface Energy Balance components (CoSEB) (Wang et al., 2025), which effectively  
98 learns the underlying physical interrelations (i.e. surface energy conservation law)  
99 among multiple targeted variables, provides an unprecedented opportunity to develop  
100 global datasets of land surface radiation and heat fluxes that can not only  
101 simultaneously provide high-accuracy estimates of these components but also adhere  
102 to surface radiation- and heat-conservation laws.

103 The objectives of this study are twofold: (1) to develop high-accuracy datasets of  
104 global land surface radiation and heat fluxes, which comply with the principles of  
105 radiation balance and heat balance, using our CoSEB model renewed based on in situ  
106 observations, remote sensing data and reanalysis datasets; (2) to validate the  
107 datasets/model estimates against data from in situ observations, mainstream products  
108 as well as estimates from uncoordinated random forest (RF) techniques. Section 2  
109 introduces the data resources used in this study. Section 3 briefly describes the method  
110 we used to estimate global surface radiation and heat fluxes. Section 4 presents the  
111 evaluation of the datasets/model estimates generated by our renewed CoSEB model.



112 Section 5 discusses the superiority, potential applications and uncertainties of the  
 113 developed datasets. Data availability is given in Section 6, and a summary and  
 114 conclusion is provided in Section 7.

## 115 2 Data

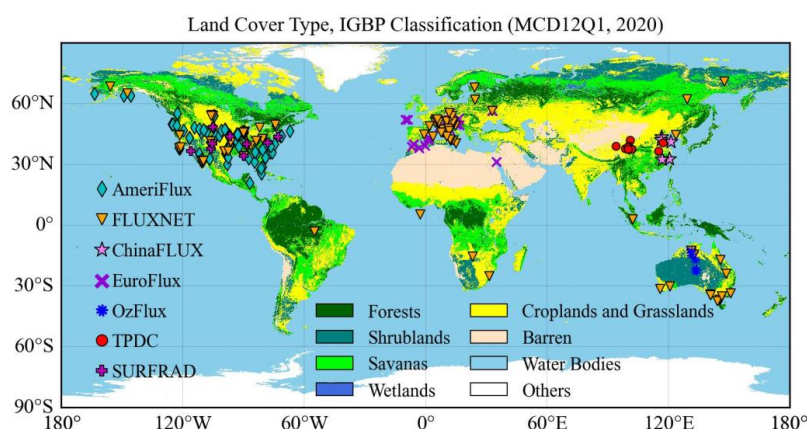
### 116 2.1 Ground-based observations

117 In this study, the in situ observations of land surface radiation and heat fluxes at  
 118 258 eddy covariance (EC) sites from the networks of AmeriFlux (145 sites, 2000–2020,  
 119 <https://AmeriFlux.lbl.gov/Data/>, last access: 6 August 2024), EuroFlux (72 sites, 2000–  
 120 2020, <http://www.europe-fluxdata.eu/>, last access: 6 August 2024), OzFlux (5 sites,  
 121 2007–2012, <https://data.ozflux.org.au/>, last access: 6 August 2024), FLUXNET (108  
 122 sites, 2000–2014, <https://FLUXNET.org/Data/download-Data/>, last access: 6 August  
 123 2024), ChinaFLUX (5 sites, 2005–2020, <http://www.chinaflux.org/>, last access: 6  
 124 August 2024) and National Tibetan Plateau/Third Pole Environment Data Center  
 125 (TPDC, 13 sites, 2012–2020, <https://Data.tpdc.ac.cn/en/Data>, last access: 6 August  
 126 2024) were used (Fig. 1), where 37, 48 and 5 sites in FLUXNET were also shared in  
 127 AmeriFlux, EuroFlux and OzFlux, respectively. These 258 sites were filtered out from  
 128 all collected 1008 sites by following the quality-assurance and quality-control steps,  
 129 including: (1) any site with a missing component of any of the  $SW_{IN}$ ,  $SW_{OUT}$ ,  $LW_{IN}$ ,  
 130  $LW_{OUT}$ , LE, H and G was excluded, reducing the 1008 sites to 388 sites for further  
 131 analysis; (2) any half-hour period with missing data for any of these components was  
 132 excluded; (3) the half-hourly ground-based observations with quality-control flag of 2  
 133 or 3 (bad quality) were removed but quality-control flag of 0 and 1 (good quality) were  
 134 maintained; (4) a daily average of the half-hour observations was calculated for each  
 135 day with greater than 80% good-quality data, further reducing the 388 sites to 286 sites;  
 136 (5) the aggregated daily LE and H were corrected for energy imbalance using the  
 137 Bowen ratio method when the daily energy balance closure [defined as  
 138  $(LE + H) / (R_n - G)$ ] varied between 0.2 and 1.8; (5) outliers were discarded,



139 corresponding to the 1 and 99 quantiles of the daily evaporation fraction, further  
 140 reducing the 286 sites to 268 sites. Besides, the RS data involved in this study collocated  
 141 at the sites should not be missing, finally reducing the 268 sites to 258 sites for analysis.  
 142 Note that the  $R_n$  at these sites used in this study was calculated from the sum of net  
 143 longwave radiation ( $LW_{IN}$  minus  $LW_{OUT}$ ) and net shortwave radiation ( $SW_{IN}$  minus  
 144  $SW_{OUT}$ ), rather than using the observed  $R_n$  directly, to ensure surface radiation balance  
 145 in training datasets.

146 These 258 sites used in this study cover a wide range of global climate regimes  
 147 across 14 land cover types, including (1) evergreen needleleaf forests (ENF, 54 sites);  
 148 (2) evergreen broadleaf forests (EBF, 11 sites); (3) deciduous needleleaf forests (DNF,  
 149 1 sites); (4) deciduous broadleaf forests (39 sites); (5) mixed forests (MF, 8 sites); (6)  
 150 closed shrublands (CSH, 5 sites); (7) open shrublands (OSH, 9 sites); (8) woody  
 151 savannas (WSA, 6 sites); (9) savannas (SAV, 10 sites); (10) grasslands (GRA, 54 sites);  
 152 (11) permanent wetlands (WET, 16 sites); (12) croplands (CRO, 43 sites); (13) water  
 153 bodies (WAT, 1 sites); (14) cropland/natural vegetation mosaics (CVM, 1 sites).



154  
 155 **Fig. 1 Spatial distribution of the 258 eddy covariance sites from AmeriFlux, FLUXNET,**  
 156 **EuroFlux, OzFlux, ChinaFLUX and TPDC, and nine radiation sites from SURFRAD involved**  
 157 **for analysis in this study.**

158 Furthermore, ground-based radiation observations from nine sites that are located  
 159 in large flat agricultural areas covered by crops and grasses from SURFRAD were also



introduced to validate land surface radiation estimates. Similar to the preprocessing performed on the observations of the 258 EC sites, the  $SW_{IN}$ ,  $SW_{OUT}$ ,  $LW_{IN}$ ,  $LW_{OUT}$  and  $R_n$  from the SURFRAD were also quality-controlled and aggregated to daily data. Spatial distribution of the 258 EC sites and nine radiation sites from SURFRAD are shown in Fig. 1, with site details (latitude, longitude, land cover types, digital elevation model and temporal coverage) provided in Supplementary Tables S1 and S2.

**Table 1 Summary of mainstream datasets/products for inter-comparison used in this study**

Products/ datasets	Reso- lution	Time coverage	Variables	Algorithms	References
GLASS	0.05°/ daily	2000- 2018	$SW_{IN}$ , $LW_{IN}$ , $LW_{OUT}$ , $R_n$	Machine learning, direct estimation algorithm	Wang et al. (2015); Xu et al. (2022b); Jiang et al. (2015)
BESS-Rad	0.05°/ daily	2000- 2020	$SW_{IN}$	BESS process model	Ryu et al. (2018)
BESSV2.0	0.05°/ daily	2000- 2020	$R_n$ , LE	BESS process model	Li et al. (2023)
FLUXCOM	0.0833°/ 8-day	2000- 2020	$R_n$ , LE, H	Model tree ensembles	Jung et al. (2019)
MOD16A2	500 m/ 8-day	2000- 2020	$R_n$ , LE	Modified Penman- Monteith equation Penman Monteith- Leuning model,	Mu et al. (2011)
PML_V2	500 m/ 8-day	2002- 2020	LE	Priestly Taylor equation and Gash model Shuttleworth- Wallace two- source scheme,	Zhang et al. (2019)
ETMonitor	1 km/ daily	2000- 2020	LE	Gash model and Penman equation	Zheng et al. (2022)

## 2.2 Climate/meteorology and remote sensing data

To generate global datasets of land surface radiation and heat fluxes from 2000 to 2020, five types of climate/meteorology and remote sensing data were used in this study, including:



- 171 (1) ERA5-Land reanalysis datasets (<https://cds.climate.copernicus.eu/>, last access: 6  
 172 August 2024) with the spatial resolution of ~9 km from 1950 (Muñoz-Sabater et  
 173 al., 2021). Following our previous work (Wang et al., 2025), this study used  
 174 variables from the ERA5-Land datasets to drive the model, including near-surface  
 175 2 m air temperature ( $T_a$ ), soil temperature in layer 1 (0-7 cm,  $T_{s1}$ ), soil volumetric  
 176 moisture content in layer 1 (0-7 cm,  $SM1$ ), solar radiation reaching the surface  
 177 of the earth ( $SW_{IN}^{ERA5}$ ), net thermal radiation at the surface ( $LW_{net}$ ), pressure of the  
 178 atmosphere ( $PA$ ), 10 m wind speed ( $WS$ ), precipitation ( $P_r$ ) and the 2 m  
 179 dewpoint temperature, daily minimum and maximum air temperature [for  
 180 calculating relative air humidity ( $RH$ )].
  - 181 (2) GLASS datasets (<https://glass.bnu.edu.cn/>, last access: 6 August 2024), which  
 182 provide the 500 m 8-day leaf area index ( $LAI$ ) and fractional vegetation cover  
 183 ( $FVC$ ) from February 2000 to December 2021.
  - 184 (3) MOD44B product (<https://lpdaac.usgs.gov/>, last access: 6 August 2024), which  
 185 offers yearly 250 m percent tree cover ( $PTC$ ) since 2000, representing the  
 186 percentage (0~100%) of a pixel covered by tree canopy.
  - 187 (4) NOAA/GML atmospheric carbon dioxide ( $CO_2$ ) concentration data, providing  
 188 monthly global marine surface mean data since 1958  
 189 ([ftp://aftp.cmdl.noaa.gov/products/trends/co2/co2\\_mm\\_gl.txt](ftp://aftp.cmdl.noaa.gov/products/trends/co2/co2_mm_gl.txt), last access: 6  
 190 August 2024).
  - 191 (5) GMTED2010 topographic data  
 192 ([https://topotools.cr.usgs.gov/gmted\\_viewer/gmted2010\\_global\\_grids.php](https://topotools.cr.usgs.gov/gmted_viewer/gmted2010_global_grids.php), last  
 193 access: 6 August 2024), providing 500 m digital elevation model (DEM), slope,  
 194 and aspect.
- 195 The ~9 km ERA5-Land datasets were spatially interpolated to 500 m using the  
 196 cubic convolution method, and the 250 m  $PTC$  was resampled to 500 m using the  
 197 arithmetic averaging method.





### 2.3 Mainstream datasets/products for inter-comparison

Mainstream RS-based datasets/products of moderate-resolution global land surface radiation and heat fluxes were collected for inter-comparison (Table 1), including (1) the daily  $0.05^\circ$  GLASS  $SW_{IN}$ ,  $LW_{IN}$ ,  $LW_{OUT}$  and Rn products from 2000 to 2018 (<https://glass.bnu.edu.cn/>, last access: 6 August 2024), (2) the daily  $0.05^\circ$  Breathing Earth System Simulator Radiation (BESS-Rad)  $SW_{IN}$  products from 2000 to 2020 (<https://www.environment.snu.ac.kr/bess-rad>), (3) the daily  $0.05^\circ$  BESS Version2.0 (BESSV2.0) Rn and LE products from 2000 to 2020 (<https://www.environment.snu.ac.kr/bessv2>), (4) the 8-day  $0.0833^\circ$  FLUXCOM Rn, LE and H products from 2001 to 2020 (<https://fluxcom.org/>, last access: 6 August 2024), (5) the daily 1 km ETMonitor LE product from 2000 to 2020 (<https://data.casearth.cn/>, last access: 6 August 2024), (6) the 8-day 500 m Penman-Monteith-Leuning Version2 (PML\_V2, <https://www.tpdac.ac.cn/>, last access: 6 August 2024) LE product from 2000 to 2020; and (7) the 8-day 500 m MOD16A2 (<https://lpdaac.usgs.gov/>, last access: 6 August 2024) LE product from 2000 to 2020.

The GLASS  $SW_{IN}$  products are derived from a combination of the GLASS broadband albedo product and the surface shortwave net radiation estimates, where the surface shortwave net radiation is estimated using linear regression with MODIS top-of-atmosphere (TOA) spectral reflectance (Wang et al., 2015). The GLASS  $LW_{IN}$  and  $LW_{OUT}$  products are generated using densely connected convolutional neural networks, incorporating Advanced Very High-Resolution Radiometer (AVHRR) TOA reflectance and ERA5 near-surface meteorological data (Xu et al., 2022b). The GLASS Rn products are estimated from the meteorological variables from MERRA2 and surface variables from GLASS using the multivariate adaptive regression splines model (Jiang et al., 2015). The BESS-Rad and BESSV2.0 estimate  $SW_{IN}$  and Rn using a radiative transfer model (i.e. Forest Light Environmental Simulator, FLiES) with an artificial neural network based on MODIS and MERRA2 reanalysis datasets, and using FLiES based on MODIS products and NCEP/NCAR reanalysis data, respectively (Li et al.,



226 2023; Ryu et al., 2018). Moreover, the BESSV2.0 (Li et al., 2023), MOD16A2 (Mu et  
 227 al., 2011), PML\_V2 (Zhang et al., 2019) and ETMonitor (Zheng et al., 2022) generated  
 228 global LE by physical models, such as Penman-Monteith equation, Priestley-Taylor  
 229 equation and/or Shuttleworth-Wallace two-source scheme. The FLUXCOM Rn, LE and  
 230 H datasets are obtained through multiple machine learning methods based on in situ  
 231 observations from FLUXNET and remote sensing and meteorological data (Jung et al.,  
 232 2019). For better consistency, RF-based 8-day 0.0833° Rn and Bowen ratio-corrected  
 233 LE and H for the periods of 2000 to 2020 from the FLUXCOM were used in this study.

### 234 **3 Methods**

235 The method used to generate global datasets of land surface radiation and heat  
 236 fluxes is based on the CoSEB model/framework, which was developed by our recently  
 237 published work (Wang et al., 2025) to coordinately estimate global land surface energy  
 238 balance components (including Rn, LE, H and G) using the multivariate random forest  
 239 technique, with a combination of MODIS and GLASS products, ERA5-Land reanalysis  
 240 datasets, and in situ observations at 336 EC sites from the FLUXNET, AmeriFlux,  
 241 ChinaFLUX, EuroFlux, OzFlux and Heihe River Basin flux network. The CoSEB  
 242 model was demonstrated to be able to produce high-accuracy estimates of land surface  
 243 energy components, with the RMSE of <17 W/m<sup>2</sup> for estimating 4-day Rn, LE and H,  
 244 and the RMSE of <5 W/m<sup>2</sup> for estimating 4-day G. The most praiseworthy superiority  
 245 of the CoSEB model lies in its ability to balance the land surface energy components,  
 246 with an energy imbalance ratio [EIR, defined as  $100\% \times (Rn - G - LE - H) / Rn$ ] of 0.

247 To coordinately estimate land surface radiation and heat fluxes that comply with  
 248 both radiation balance and heat balance, one of the key procedures in the construction  
 249 of the CoSEB model was to prepare training datasets that satisfy surface radiation and  
 250 heat balance. For this purpose, the energy-imbalance corrections on daily in situ  
 251 observed LE and H were conducted by the most widely applied Bowen ratio method

$$252 \quad [H^{corr} = \frac{H}{H + LE} \times (Rn - G), \quad LE^{corr} = \frac{LE}{H + LE} \times (Rn - G)], \text{ where } H^{corr} \text{ and } LE^{corr}$$



represent the sensible heat flux and latent heat flux after energy-imbalance correction, respectively] with the aid of  $R_n$  and  $G$  observations, and the in situ  $R_n$  was calculated from the sum of in situ observed net longwave radiation ( $LW_{IN}$  minus  $LW_{OUT}$ ) and net shortwave radiation ( $SW_{IN}$  minus  $SW_{OUT}$ ). The input variables to renew the CoSEB model include: (1) climate/meteorology:  $T_a$ ,  $SW_{IN}^{ERA5}$ ,  $LW_{net}$ ,  $WS$ ,  $PA$ ,  $P_r$ ,  $RH$ ,  $CO_2$  concentration; (2) vegetation and soil:  $LAI$ ,  $FVC$ ,  $PTC$ ,  $T_{s1}$ ,  $SM1$ ; (3) topography data:  $DEM$ ,  $Slope$  and  $Aspect$ , in addition to longitude ( $Lon$ ), latitude ( $Lat$ ), and inverse relative distance from the Earth to the Sun ( $dr$ ), in which the  $dr$  was calculated as

$$dr = 1 + 0.033 \times \cos\left(\frac{2\pi \times DOY}{365}\right), \text{ where } DOY \text{ represents the day of year. Considering}$$

that the footprint of the site-based measurements of turbulent heat fluxes is generally at a scale of hundreds of meters, to reduce the effect of differences of spatial scales between ground-based measurements (dependent variables) and remotely sensed/reanalysis datasets (independent variables), we renewed the CoSEB model at a spatial scale of 500 m for coordinately estimating global daily land surface radiation and heat fluxes, which can be expressed as follows:

$$\begin{pmatrix} SW_{IN}, SW_{OUT}, LW_{IN}, \\ LW_{OUT}, R_n, LE, H, G \end{pmatrix} = f \left( \begin{pmatrix} Lon, Lat, T_a, T_{s1}, SM1, SW_{IN}^{ERA5}, LW_{net}, PA, WS, P_r, dr \\ RH, LAI, FVC, PTC, DEM, Slope, Aspect, CO_2 \end{pmatrix} \right) \quad (1)$$

For comparison, eight RF-based uncoordinated models for separate estimates of  $SW_{IN}$ ,  $SW_{OUT}$ ,  $LW_{IN}$ ,  $LW_{OUT}$ ,  $R_n$ ,  $LE$ ,  $H$  and  $G$  were also constructed using the same inputs as those in the renewed CoSEB model. Site-based 10-fold cross-validation was employed to assess the transferability and generalization of the CoSEB model by randomly dividing all sites into ten folds, where each fold in turn serves as validation datasets while the other folds as the training datasets, ensuring the validation of the estimates of the CoSEB was conducted at sites that are spatially independent from those selected for the training datasets. Fig. 2 illustrates the flowchart for generating global datasets of land surface radiation and heat fluxes by the CoSEB model.

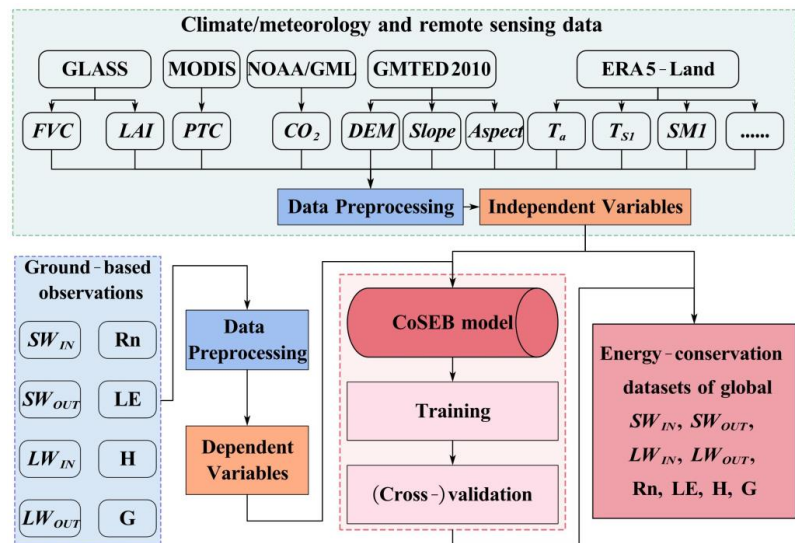


**Fig. 2** Flowchart for generating energy-conservation datasets of global land surface radiation [including downward shortwave radiation ( $SW_{IN}$ ), downward longwave radiation ( $LW_{IN}$ ), upward shortwave radiation ( $SW_{OUT}$ ), upward longwave radiation ( $LW_{OUT}$ ) and net radiation ( $R_n$ )] and heat fluxes [including latent heat flux (LE), soil heat flux (G) and sensible heat flux (H)] by the CoSEB model renewed from in situ observations at 258 sites worldwide and collocated remote sensing and reanalysis datasets.

## 4 Results

### 4.1 Validation of the CoSEB model

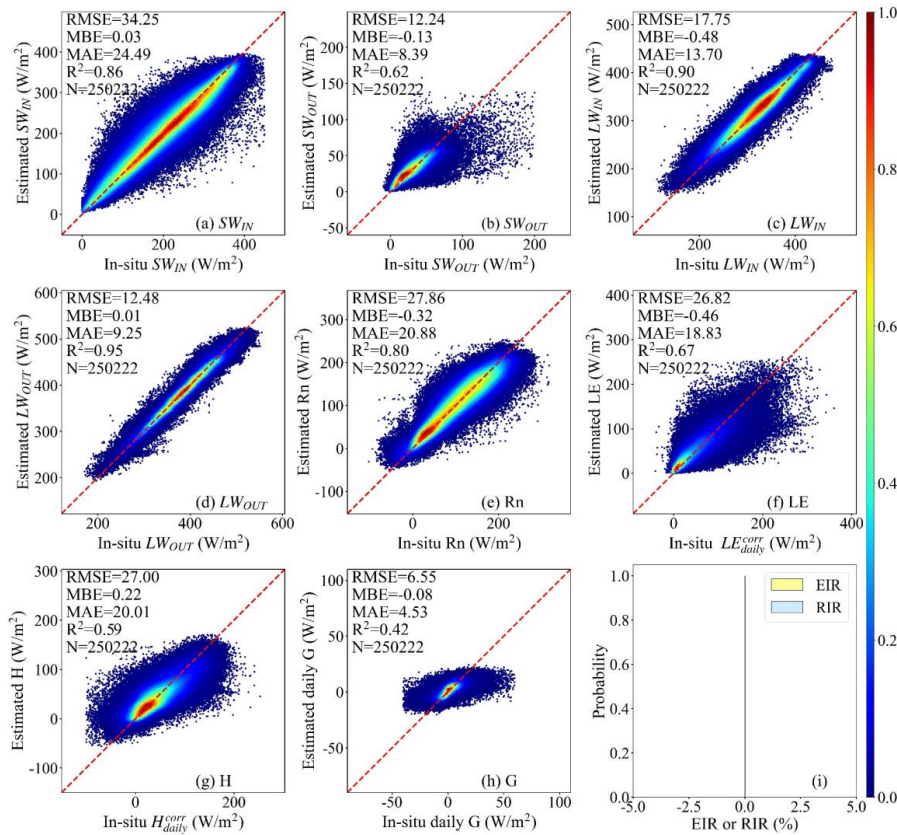
#### 4.1.1 Site-based 10-fold cross-validations at 258 EC sites

Fig. 3 and Fig. 4 present the scatter density plots of the site-based 10-fold cross-validation of daily  $SW_{IN}$ ,  $LW_{IN}$ ,  $SW_{OUT}$ ,  $LW_{OUT}$ ,  $R_n$ , LE, H and G estimated from the renewed CoSEB model and the RF-based uncoordinated models, respectively, by using the validation datasets collected at 258 EC sites worldwide. Results indicated that the estimates from both the CoSEB model and the RF-based uncoordinated models agreed well with the in situ observations, with the coefficient of determination ( $R^2$ ) varying between 0.80 and 0.95 for  $SW_{IN}$ ,  $LW_{IN}$ ,  $LW_{OUT}$  and  $R_n$ , and between 0.59 and 0.67 for  $SW_{OUT}$ , LE and H. The CoSEB model, with the root mean square error (RMSE) of 26.82 to 34.25  $W/m^2$  and mean absolute error (MAE) of 18.83 to 24.49  $W/m^2$  for  $SW_{IN}$ ,  $R_n$ , LE and H, the RMSE of 12.24 to 17.75  $W/m^2$  and the MAE of 8.39 to 13.70  $W/m^2$  for



298  $SW_{OUT}$ ,  $LW_{IN}$  and  $LW_{OUT}$ , demonstrated comparable accuracies to the RF-based models,  
 299 with the RMSE of 27.07 to 33.34 W/m<sup>2</sup> and MAE of 19.29 to 23.64 W/m<sup>2</sup> for  $SW_{IN}$ ,  
 300  $R_n$ ,  $LE$  and  $H$ , the RMSE of 12.12 to 16.93 W/m<sup>2</sup> and the MAE of 8.68 to 12.99 W/m<sup>2</sup>  
 301 for  $SW_{OUT}$ ,  $LW_{IN}$  and  $LW_{OUT}$ . In the validation of daily  $G$ , both the CoSEB and RF-based  
 302 models yielded RMSEs below 7 W/m<sup>2</sup>. Strikingly, the CoSEB model exhibited large  
 303 superiority in balancing the surface radiation and heat fluxes, with the radiation  
 304 imbalance ratio [RIR, defined as  $100\% \times (SW_{IN} + LW_{IN} - SW_{OUT} - LW_{OUT} - R_n) / R_n$ ]  
 305 and energy imbalance ratio [EIR, defined as  $100\% \times (R_n - G - LE - H) / R_n$ ] of 0,  
 306 while the RF-based uncoordinated models showed substantial imbalances of the surface  
 307 radiation and heat fluxes, with RIR and EIR that were approximately normally  
 308 distributed, having absolute mean values of 38.84% and 31.22%, respectively, and  
 309 reaching as high as 50% in some cases.

310 It should be pointed out that the performances of both the renewed CoSEB model  
 311 and the RF-based models could be further improved if the site-based 10-fold cross-  
 312 validation was replaced with the sample-based 10-fold cross-validation (Figs. S1 and  
 313 S2 in the Supplementary Material). Specifically, for the CoSEB model, using the  
 314 sample-based 10-fold cross-validation decreased the RMSE by 0.61 to 3.92 W/m<sup>2</sup> for  
 315 five radiation components and  $G$ , and by 6.25 W/m<sup>2</sup> and 5.50 W/m<sup>2</sup> for  $LE$  and  $H$ ,  
 316 respectively, in comparison to using the site-based 10-fold cross-validation. Likewise,  
 317 for the RF-based models, the RMSE decreased by 1.41 to 5.25 W/m<sup>2</sup> for five radiation  
 318 components and  $G$ , and by 9.63 W/m<sup>2</sup> and 7.43 W/m<sup>2</sup> for  $LE$  and  $H$ , respectively. The  
 319  $R^2$  of both the CoSEB model and the RF-based models using the sample-based 10-fold  
 320 cross-validation increased by 0.02 to 0.28 compared to the  $R^2$  using the site-based 10-  
 321 fold cross-validation.



**Fig. 3** Scatter density plots of the site-based 10-fold cross-validation of daily downward shortwave and longwave radiation ( $SW_{IN}$  and  $LW_{IN}$ ), upward shortwave and longwave radiation ( $SW_{OUT}$  and  $LW_{OUT}$ ), net radiation ( $Rn$ ), soil heat flux ( $G$ ), latent heat flux ( $LE$ ) and sensible heat flux ( $H$ ) derived by the CoSEB model against in situ observed  $SW_{IN}$ ,  $LW_{IN}$ ,  $SW_{OUT}$ ,  $LW_{OUT}$ ,  $Rn$ ,  $G$ , and energy imbalance-corrected  $LE$  ( $LE^{corr}_{daily}$ ) and  $H$  ( $H^{corr}_{daily}$ ). The EIR and RIR in the subfigure (i) represent the energy imbalance ratio and radiation imbalance ratio, which are defined as  $100\% \times (Rn - G - LE - H) / Rn$  and  $100\% \times (SW_{IN} + LW_{IN} - SW_{OUT} - LW_{OUT} - Rn) / Rn$ , respectively. The colorbar represents the normalized density of data points.



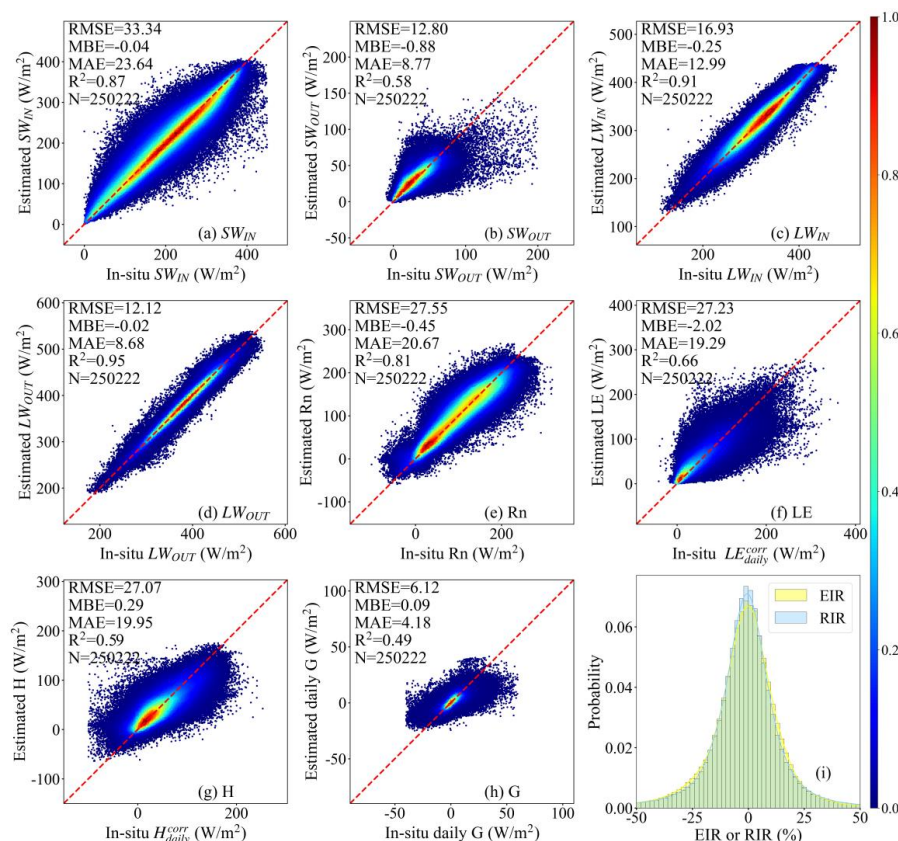


**Fig. 4** Same as Fig. 3, but for estimates from RF-based uncoordinated models.

#### 4.1.2 Validation at nine radiation sites from SURFRAD

To further illustrate the generality and transferability of the renewed CoSEB model, the validation of estimates of the five radiation components (including  $SW_{IN}$ ,  $SW_{OUT}$ ,  $LW_{IN}$ ,  $LW_{OUT}$ ,  $Rn$ ) derived from both the CoSEB model and RF-based uncoordinated models against observations at nine radiation sites from SURFRAD was performed, as shown in Fig. 5. The results showed that both the CoSEB model and the RF-based models achieved high accuracy in estimating daily  $SW_{IN}$ ,  $SW_{OUT}$ ,  $LW_{IN}$ ,  $LW_{OUT}$  and  $Rn$ , with the RMSE of  $\sim 30$   $W/m^2$  for  $SW_{IN}$ ,  $\sim 14$   $W/m^2$  for  $SW_{OUT}$  and  $LW_{IN}$ ,  $\sim 12$   $W/m^2$  for  $LW_{OUT}$  and  $\sim 24$   $W/m^2$  for  $Rn$ , with the  $R^2 > 0.9$  for  $SW_{IN}$ ,  $LW_{IN}$  and  $LW_{OUT}$ ,  $\sim 0.65$  for  $SW_{OUT}$  and  $\sim 0.85$  for  $Rn$ . Compared to the results of the site-based 10-fold cross-validation at 258 EC sites, the performances at nine radiation sites showed slight



345 improvements, with the RMSE decreasing by 0.74 to 4.54 W/m<sup>2</sup> for  $SW_{IN}$ ,  $LW_{IN}$ ,  $LW_{OUT}$   
346 and  $R_n$  in the CoSEB model, but a slight degradation with the RMSE increasing by  
347  $\sim 1.05$  W/m<sup>2</sup> for  $SW_{OUT}$ , suggesting the robust performance of the CoSEB model.  
348 Furthermore, the CoSEB model demonstrated a large superiority in maintaining surface  
349 radiation balance among the five radiation components, with the RIR of 0, in contrast  
350 to the RF-based models, which failed to meet this balance, exhibiting significant RIR  
351 exceeding 50%.

352



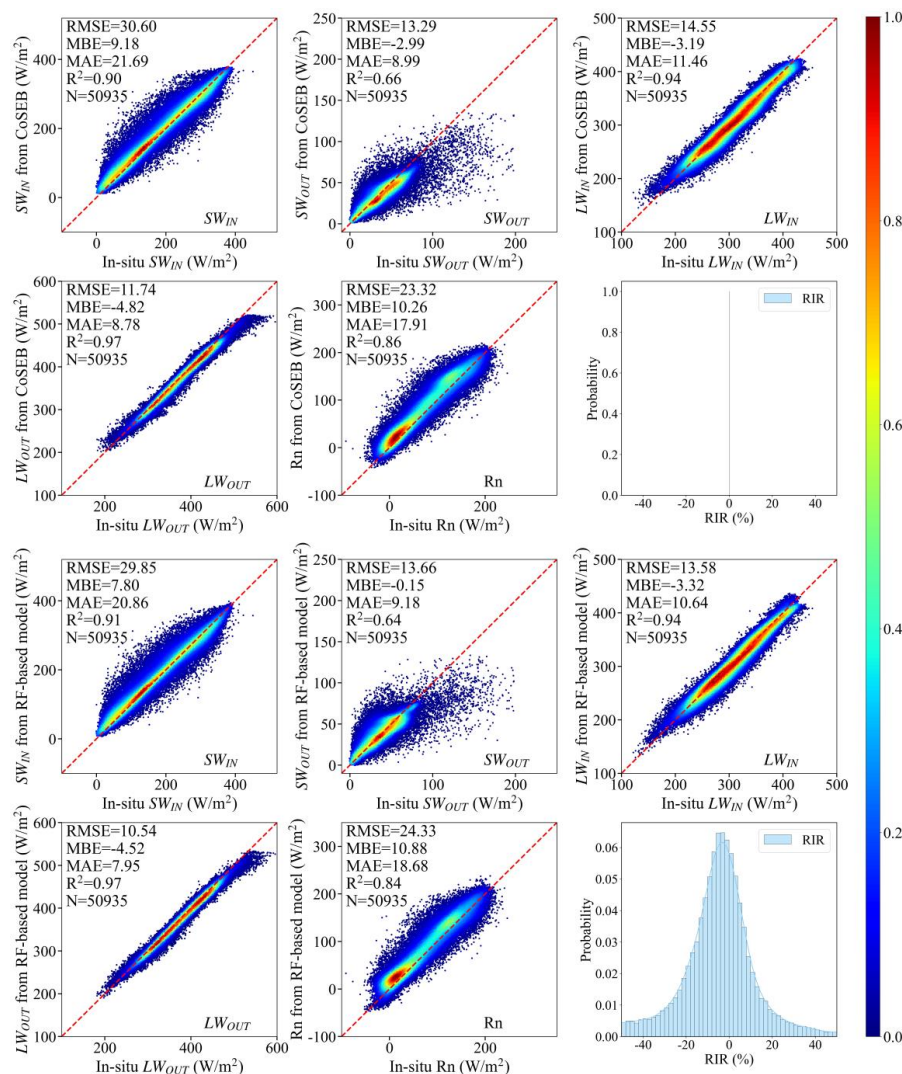


**Fig. 5** Scatter density plots of the validation of daily downward shortwave and longwave radiation ( $SW_{IN}$  and  $LW_{IN}$ ), upward shortwave and longwave radiation ( $SW_{OUT}$  and  $LW_{OUT}$ ) and net radiation ( $Rn$ ) from the CoSEB-based datasets against in situ observations at nine radiation sites from SURFRAD. The RIR represents the radiation imbalance ratio, defined as  $100\% \times (SW_{IN} + LW_{IN} - SW_{OUT} - LW_{OUT} - Rn) / Rn$ . The colorbar represents the normalized density of data points.

#### 4.2 Validation and inter-comparisons of the CoSEB-based datasets

As demonstrated in Section 4.1, the renewed CoSEB model with a spatial scale of 500 m achieved comparable accuracies to the RF-based uncoordinated models but



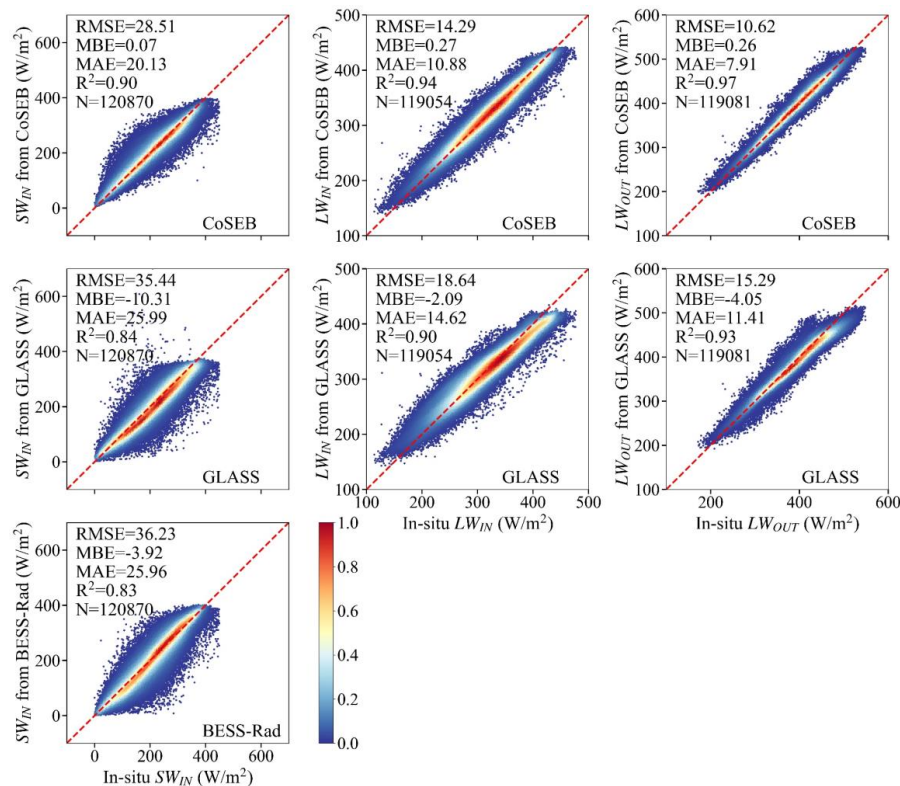
363 outperformed them in balancing surface radiation and heat fluxes. Evidenced by the  
 364 validation for its superiority, the renewed CoSEB model was then applied to the  
 365 spatially aggregated input datasets to generate our developed global daily datasets with  
 366 a spatial resolution of  $0.05^\circ$ . To further assess the performance of the developed datasets,  
 367 in situ observations at 134 sites out of the 258 EC sites were further used to test the  
 368 performance of the CoSEB-based datasets, where the 134 sites were selected based on  
 369 the commonly applied criterion (Salazar-Martínez et al., 2022; Tang et al., 2024a) that  
 370 the fraction of the dominant land cover types (from the 500 m MCD12Q1 product)  
 371 exceeded 80% within the  $0.05^\circ$  grid, ensuring surface homogeneity and spatial  
 372 representativeness of the observations. Mainstream products (i.e. GLASS, BESS-Rad,  
 373 BESSV2.0, FLUXCOM, PML\_V2, MOD16A2 and ETMonitor) were also involved for  
 374 inter-comparison at the 134 EC sites.

375 Note that due to the lack of moderate-resolution global RS-based products/datasets  
 376 of daily and/or 8-day  $SW_{OUT}$ ,  $H$  and  $G$ , the intercomparison between different  
 377 products/datasets was impossible. Instead, we conducted a validation of these  
 378 components from the CoSEB-based datasets against in situ observations at 134 EC sites,  
 379 as shown in Figs S3 and S4 in the Supplementary Material. Results indicated that the  
 380 CoSEB-based datasets could provide good estimates of  $SW_{OUT}$ ,  $H$  and  $G$ , with the  
 381 RMSE of  $10.39 \text{ W/m}^2$ ,  $22.67 \text{ W/m}^2$  and  $6.77 \text{ W/m}^2$  at daily scale, respectively, and the  
 382 RMSE of  $7.08 \text{ W/m}^2$  and  $4.25 \text{ W/m}^2$  for 8-day  $SW_{OUT}$  and  $G$ , respectively.

383 Fig. 6 and Fig. 7 present the comparison of daily  $SW_{IN}$ ,  $LW_{IN}$  and  $LW_{OUT}$ , as well  
 384 as  $R_n$  and  $LE$  from the CoSEB-based datasets and mainstream products/datasets  
 385 (including GLASS, BESS-Rad, BESSV2.0 and ETMonitor), with in situ observations  
 386 at 134 EC sites, respectively. Overall, the estimates from the CoSEB-based datasets  
 387 exhibited a closer agreement with in situ observations than those from mainstream  
 388 products/datasets, where the CoSEB-based datasets reduced the RMSE by  $4.35 \text{ W/m}^2$   
 389 to  $11.46 \text{ W/m}^2$  and increased the  $R^2$  by 0.04 to 0.3 compared to mainstream products.  
 390 Specifically, the RMSE for the  $SW_{IN}$ ,  $LW_{IN}$ ,  $LW_{OUT}$  increased from  $28.51 \text{ W/m}^2$ ,  $14.29$



391  $\text{W/m}^2$  and  $10.62 \text{ W/m}^2$  in the CoSEB-based datasets to  $35.44 \text{ W/m}^2$ ,  $18.64 \text{ W/m}^2$  and  
 392  $15.29 \text{ W/m}^2$  in the GLASS, respectively, and for  $SW_{IN}$  from  $28.51 \text{ W/m}^2$  in the CoSEB-  
 393 based datasets to  $36.23 \text{ W/m}^2$  in the BESS-Rad. Likewise, the RMSEs for daily Rn and  
 394 LE were  $22.40 \text{ W/m}^2$  and  $24.38 \text{ W/m}^2$  in the CoSEB-based datasets, which were lower  
 395 than those of  $29.80 \text{ W/m}^2$  and  $35.75 \text{ W/m}^2$  in BESSV2.0, respectively, as well as those  
 396 of  $27.11 \text{ W/m}^2$  for Rn in GLASS and  $35.84 \text{ W/m}^2$  for LE in ETMonitor.



397  
 398 **Fig. 6** Comparison of the daily downward shortwave radiation ( $SW_{IN}$ , the first column),  
 399 downward longwave radiation ( $LW_{IN}$ , the second column) and upward longwave radiation  
 400 ( $LW_{OUT}$ , the third column) from the CoSEB-based datasets, GLASS and BESS-Rad with the  
 401 in situ observed  $SW_{IN}$ ,  $LW_{IN}$  and  $LW_{OUT}$  at 134 eddy covariance sites. The colorbar represents  
 402 the normalized density of data points.

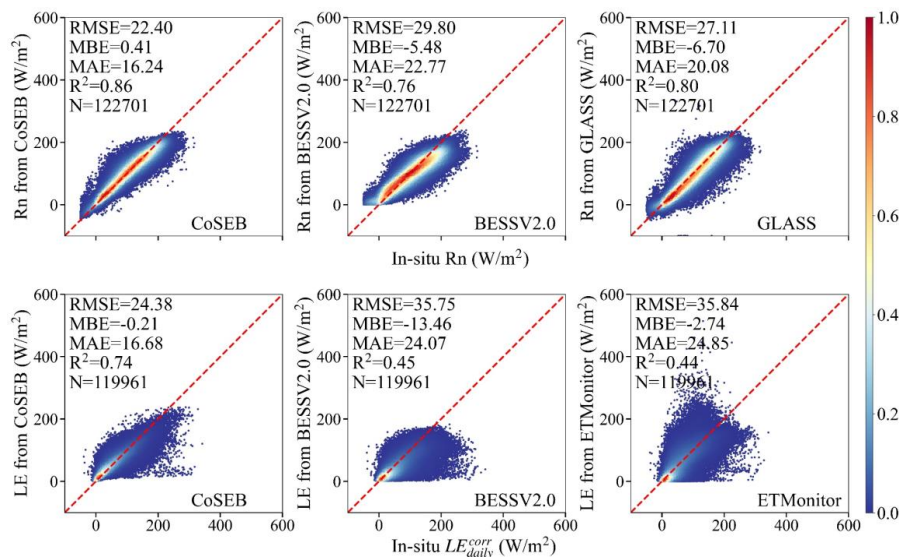


**Fig. 7** Comparison of the daily net radiation (Rn, the upper row) and latent heat flux (LE, the lower row) from the CoSEB-based datasets, BESSV2.0, GLASS and ETMonitor with the in situ observed Rn, and energy imbalance-corrected LE ( $LE_{daily}^{corr}$ ) at 134 eddy covariance sites. The colorbar represents the normalized density of data points.

Figs. 8, 9 and 10 compare the 8-day  $SW_{IN}$ ,  $LW_{IN}$  and  $LW_{OUT}$ , Rn and LE, as well as H from the CoSEB-based datasets and mainstream products, with in situ observations at 134 EC sites, respectively. Overall, the CoSEB-based datasets outperformed the mainstream products/datasets for all surface radiation and heat fluxes, where the CoSEB-based datasets reduced the RMSE by 4.62 W/m<sup>2</sup> to 14.64 W/m<sup>2</sup> and increased the R<sup>2</sup> by 0.04 to 0.41 compared to mainstream products. Specifically, for  $SW_{IN}$ ,  $LW_{IN}$  and  $LW_{OUT}$ , the RMSE increased from 12.81 W/m<sup>2</sup>, 9.22 W/m<sup>2</sup> and 8.34 W/m<sup>2</sup> in the CoSEB-based datasets to 21.23 W/m<sup>2</sup>, 15.37 W/m<sup>2</sup> and 14.70 W/m<sup>2</sup> in the GLASS, respectively, and for  $SW_{IN}$  from 12.81 W/m<sup>2</sup> in the CoSEB-based datasets to 17.43 W/m<sup>2</sup> in the BESS-Rad. For Rn, the RMSE increased from 13.38 W/m<sup>2</sup> in the CoSEB-based datasets to 18.64 W/m<sup>2</sup> in the GLASS and to >23 W/m<sup>2</sup> in the FLUXCOM and BESSV2.0, while the R<sup>2</sup> decreased from 0.91 in the CoSEB to 0.82 in the GLASS and to <0.72 in the FLUXCOM and BESSV2.0. Likewise, for LE, the RMSE increased from 19.99 W/m<sup>2</sup> in the CoSEB-based datasets to 26.16 W/m<sup>2</sup> in the FLUXCOM, and



to  $>28.17 \text{ W/m}^2$  in BESSV2.0, MOD16A2, PML\_V2 and ETMonitor, while the  $R^2$   
 decreased from 0.8 in the CoSEB-based datasets to 0.65 in the FLUXCOM, and to  $<0.6$   
 in the remaining products. For H, the RMSE increased from  $17.44 \text{ W/m}^2$  in the CoSEB-  
 based datasets to  $23.96 \text{ W/m}^2$  in the FLUXCOM.

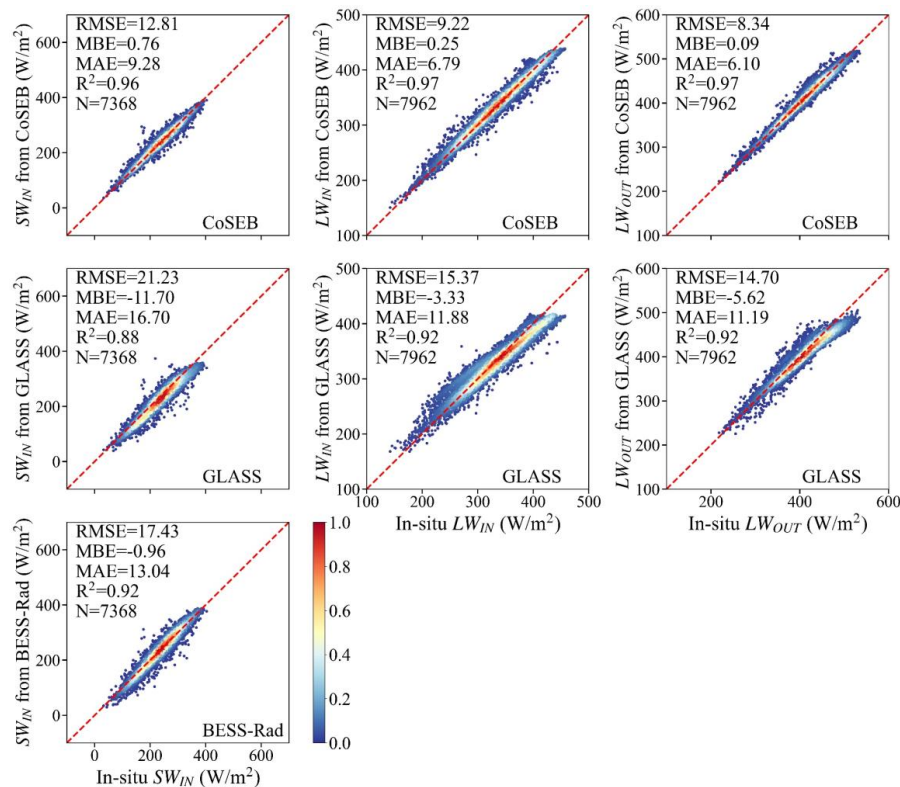
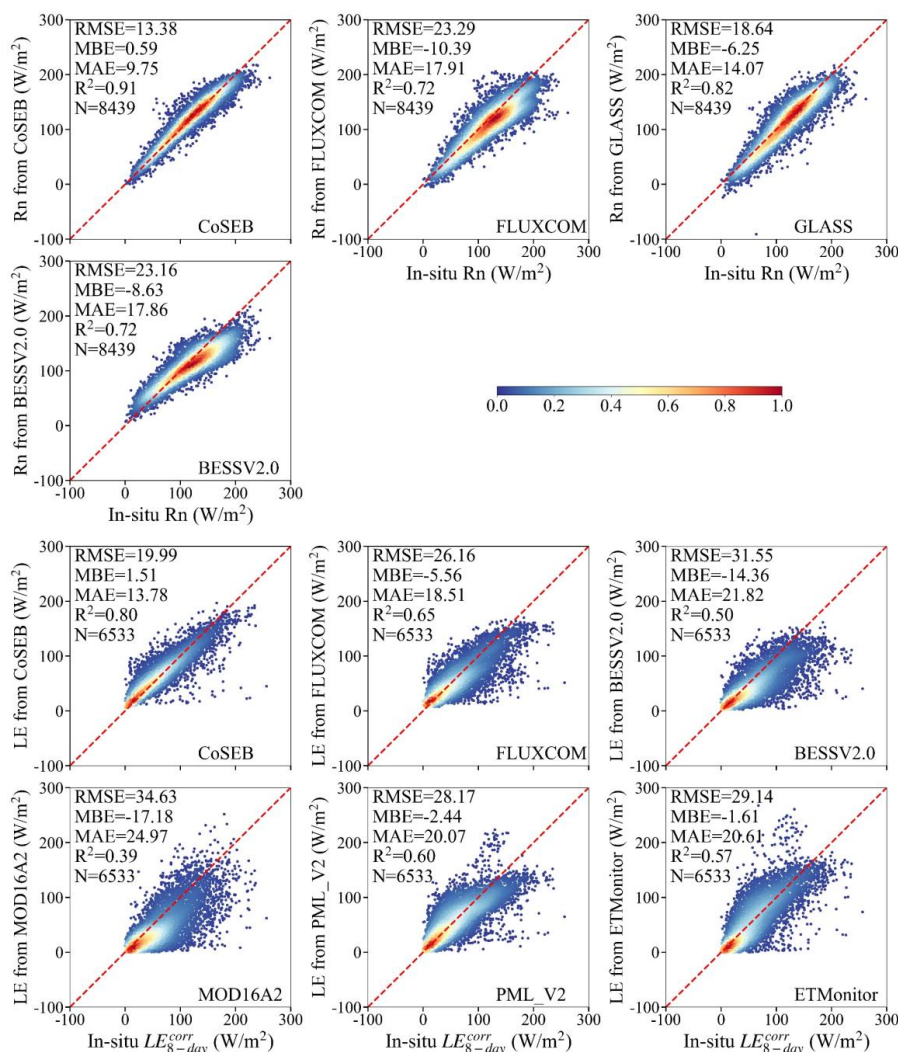
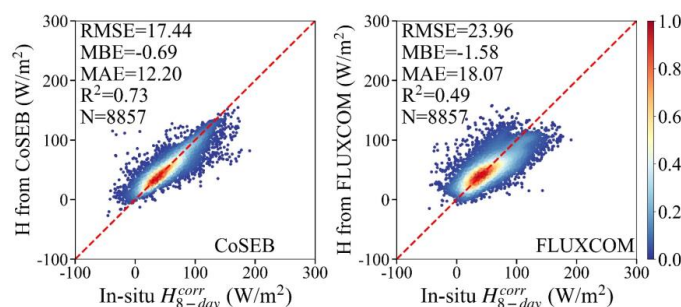


Fig. 8 Same as Fig. 6, but for the comparison at 8-day scale.





**Fig. 9** Comparison of the 8-day net radiation (Rn, the upper two rows) and latent heat flux (LE, the lower three rows) from the CoSEB-based datasets, FLUXCOM, BESSV2.0, GLASS, MOD16A2, PML\_V2 and ETMonitor with in situ observed Rn, and energy imbalance-corrected LE ( $LE_{8-day}^{corr}$ ) at 134 eddy covariance sites. The colorbar represents the normalized density of data points.



**Fig. 10 Comparison of the 8-day sensible heat flux (H) from the CoSEB-based datasets and the FLUXCOM with the in situ energy imbalance-corrected H ( $H_{8\text{-day}}^{\text{corr}}$ ) at 134 eddy covariance sites. The colorbar represents the normalized density of data points.**

### 4.3 Spatial-temporal patterns of global land surface radiation and heat fluxes

In addition to the validation and inter-comparison of the CoSEB-based datasets at global sites, we further inter-compared the estimates of land surface radiation and heat fluxes from the CoSEB-based datasets and the mainstream products/datasets, in terms of their spatial and temporal patterns.

Figs. 11, 12 and 13 show the spatial distributions (excluding Greenland, Antarctic continent, deserts, water bodies and permanent snow) and latitudinal profiles of the global  $0.05^\circ$  mean annual  $SW_{IN}$ ,  $LW_{IN}$  and  $LW_{OUT}$ , Rn and LE, as well as H from 2001 to 2018, respectively, as derived from the CoSEB-based datasets and mainstream products/datasets [i.e. GLASS, BESS-Rad, BESSV2.0, FLUXCOM, MOD16A2, PML\_V2 and ETMonitor, resampled to  $0.05^\circ$  using arithmetic averaging method or cubic convolutional method if necessary]. Overall, the spatial patterns of the estimates from the CoSEB-based datasets aligned well with those observed in these mainstream products/datasets, though regional discrepancies were present. Specifically, the mean annual  $LW_{IN}$ ,  $LW_{OUT}$ , Rn, and LE generally exhibited decreasing trends from the equator towards higher latitudes, peaking in regions such as the Amazon Rainforest, Congo Rainforest, and the Malay Archipelago. In contrast, the higher mean annual  $SW_{IN}$  and H were mainly found in the Tibetan Plateau, southwestern U.S., mid-west Australia, Sahel and Southern Africa, while the lower values were found in high-latitude regions



458 of  $>50^{\circ}\text{N}$ . In the region of high values, the mean annual estimates of  $SW_{IN}$  from the  
459 CoSEB-based datasets were higher than those from GLASS but lower than those from  
460 BESS-Rad, the estimates of  $LW_{IN}$  and  $LW_{OUT}$  from the CoSEB-based datasets were both  
461 higher than those from GLASS, the estimates of  $R_n$  from the CoSEB-based datasets  
462 were significantly higher than those from BESSV2.0, and comparable to or slightly  
463 higher than those from FLUXCOM and GLASS, the estimates of  $LE$  from the CoSEB-  
464 based datasets were close to those from BESSV2.0 and PML\_V2, but slightly lower  
465 than those from FLUXCOM, MOD16A2 and ETMonitor. Besides, the estimates of  $H$   
466 from the CoSEB-based datasets were higher than those from FLUXCOM in regions  
467 with high values, while lower than those from FLUXCOM in regions with low values.



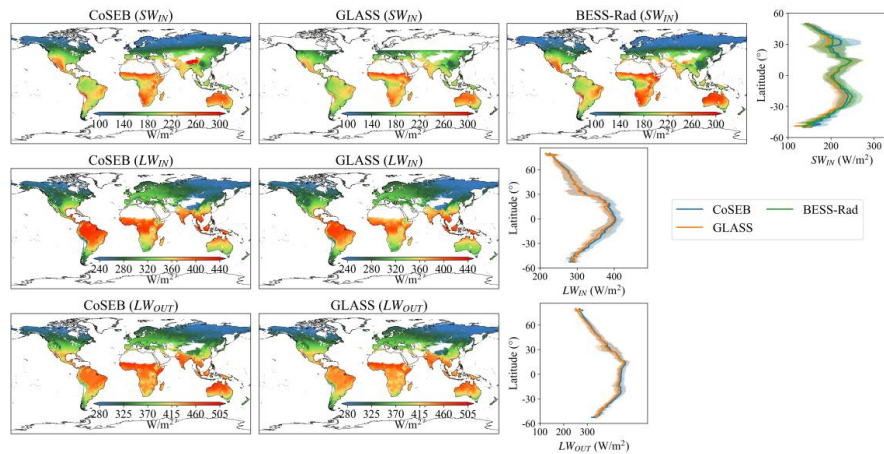


**Fig.11** Spatial patterns of global mean annual downward shortwave radiation ( $SW_{IN}$ , the first row), downward longwave radiation ( $LW_{IN}$ , the second row) and upward longwave radiation ( $LW_{OUT}$ , the third row) from 2001 to 2018 by CoSEB-based datasets, GLASS and BESS-Rad. The rightmost subfigure of each row represents the latitudinal profiles of mean annual  $SW_{IN}$ ,  $LW_{IN}$  and  $LW_{OUT}$  from CoSEB-based datasets, GLASS and BESS-Rad, where the shaded area represents the variation of standard deviation for each product.

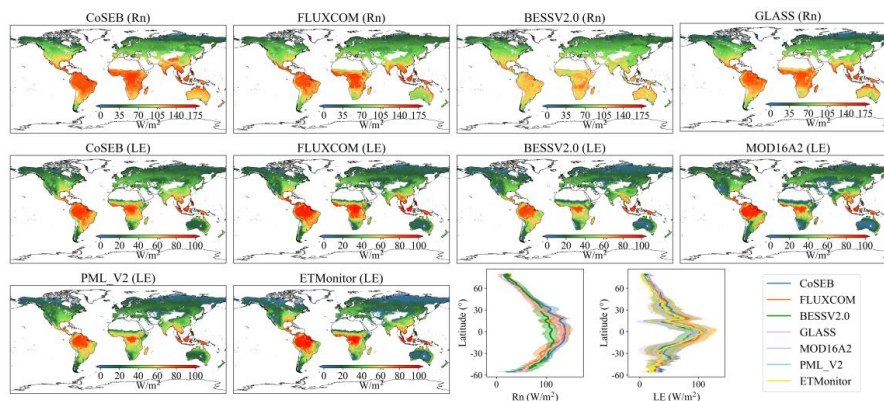


**Fig.12** Spatial patterns of global mean annual net radiation ( $Rn$ , the first row) and latent heat flux ( $LE$ , the second and third rows) from 2001 to 2018 by CoSEB-based datasets, FLUXCOM, BESSV2.0, MOD16A2, PML\_V2, ETMonitor and GLASS. The last two subfigures of the third row represent the latitudinal profiles of mean annual  $Rn$  and  $LE$  from CoSEB-based datasets and these mainstream products/datasets, where the shaded area represents the variation of standard deviation for each product.

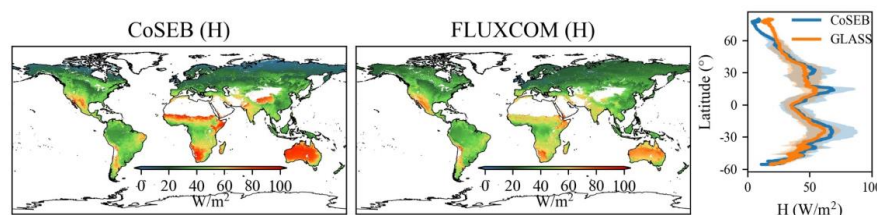
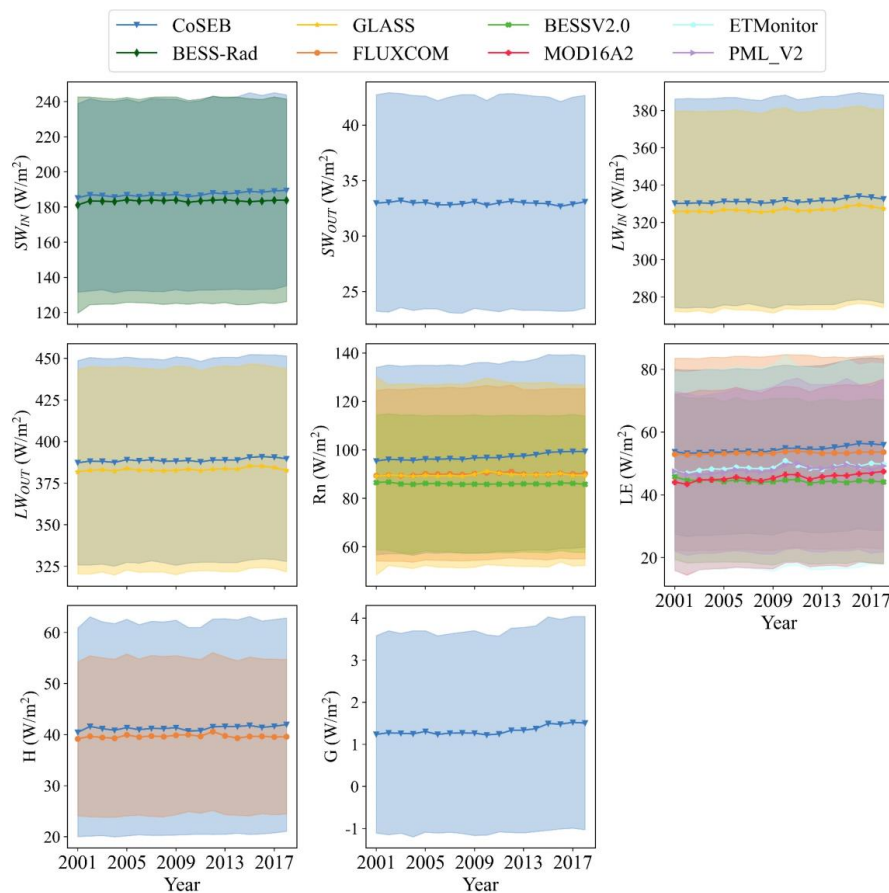


**Fig.13 Spatial patterns of global mean annual sensible heat flux ( $H$ ) from 2001 to 2018 by CoSEB-based datasets and FLUXCOM. The rightmost subfigure represents the latitudinal profiles of mean annual  $H$  from CoSEB-based datasets and FLUXCOM, where the shaded area represents the variation of standard deviation for each product.**

The temporal evolutions of the global (excluding Greenland, Antarctic continent, deserts, water bodies and permanent snow) land surface radiation and heat fluxes derived from the CoSEB-based datasets and mainstream products/datasets from 2001 to 2018 were also investigated, as shown in Fig. 14. The results indicated that the temporal variation of each flux from the CoSEB-based datasets generally agreed well with those from mainstream products/datasets, exhibiting relatively stable trends. The global annual mean estimates using area weighting average by the CoSEB-based datasets from 2001 to 2018 varied between  $\sim 185.22$  and  $\sim 189.50$   $\text{W/m}^2$  with the mean of  $\sim 187.23$   $\text{W/m}^2$  for  $SW_{IN}$ , between  $\sim 32.67$  and  $\sim 33.20$   $\text{W/m}^2$  with the mean of  $\sim 32.96$   $\text{W/m}^2$  for  $SW_{OUT}$ , between  $\sim 330.24$  and  $\sim 334.14$   $\text{W/m}^2$  with the mean of  $\sim 331.50$   $\text{W/m}^2$  for  $LW_{IN}$ , between  $\sim 387.25$  and  $\sim 390.82$   $\text{W/m}^2$  with the mean of  $\sim 388.81$   $\text{W/m}^2$  for  $LW_{OUT}$ , between  $\sim 95.41$  and  $\sim 99.39$   $\text{W/m}^2$  with the mean of  $97.11$   $\text{W/m}^2$  for  $R_n$ , between  $\sim 53.24$  and  $\sim 56.37$   $\text{W/m}^2$  with the mean of  $\sim 54.53$   $\text{W/m}^2$  for  $LE$ , between  $\sim 40.44$  and  $\sim 41.96$   $\text{W/m}^2$  with the mean of  $\sim 41.29$   $\text{W/m}^2$  for  $H$ , and between  $\sim 1.22$  and  $\sim 1.52$   $\text{W/m}^2$  with the mean of  $\sim 1.33$   $\text{W/m}^2$  for  $G$ . For each radiation or heat flux, the annual mean estimates from the CoSEB-based datasets were overall higher than those from the mainstream products/datasets. In particular, the annual mean  $R_n$  estimates from the CoSEB-based datasets were higher than those from FLUXCOM, GLASS and BESSV2.0 sequentially, and the annual mean  $LE$  estimates from the CoSEB-based datasets were marginally higher than those from FLUXCOM, but substantially exceeded those from ETMonitor, PML\_V2, MOD16A2 and BESSV2.0 sequentially.



508  
 509 **Fig. 14** Temporal variation of annual mean downward shortwave radiation ( $SW_{IN}$ ), upward  
 510 shortwave radiation ( $SW_{OUT}$ ), downward longwave radiation ( $LW_{IN}$ ), upward longwave  
 511 radiation ( $LW_{OUT}$ ), net radiation ( $R_n$ ), latent heat flux ( $LE$ ), sensible heat flux ( $H$ ) and soil heat  
 512 flux ( $G$ ) from 2001 to 2018 from the CoSEB-based datasets, BESS-Rad, GLASS, FLUXCOM,  
 513 BESSV2.0, PML\_V2, MOD16A2 and ETMonitor. The shaded area represents the variation of  
 514 standard deviation for each product.

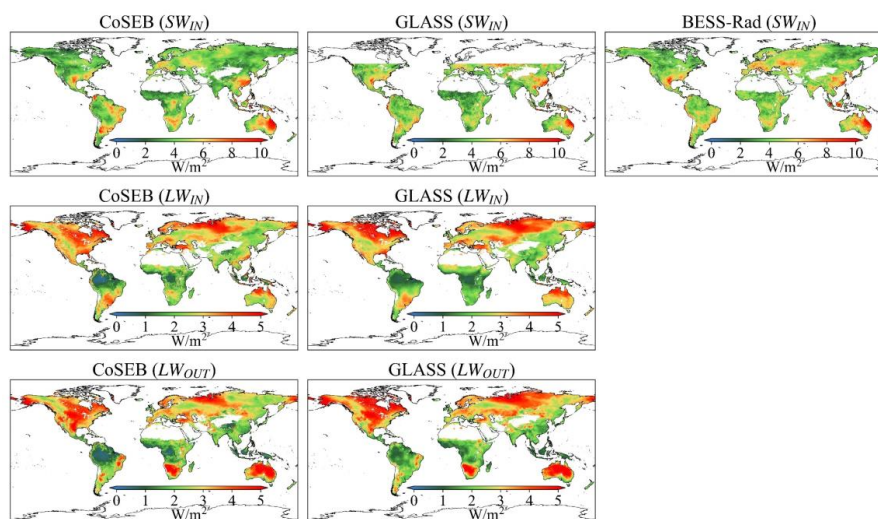
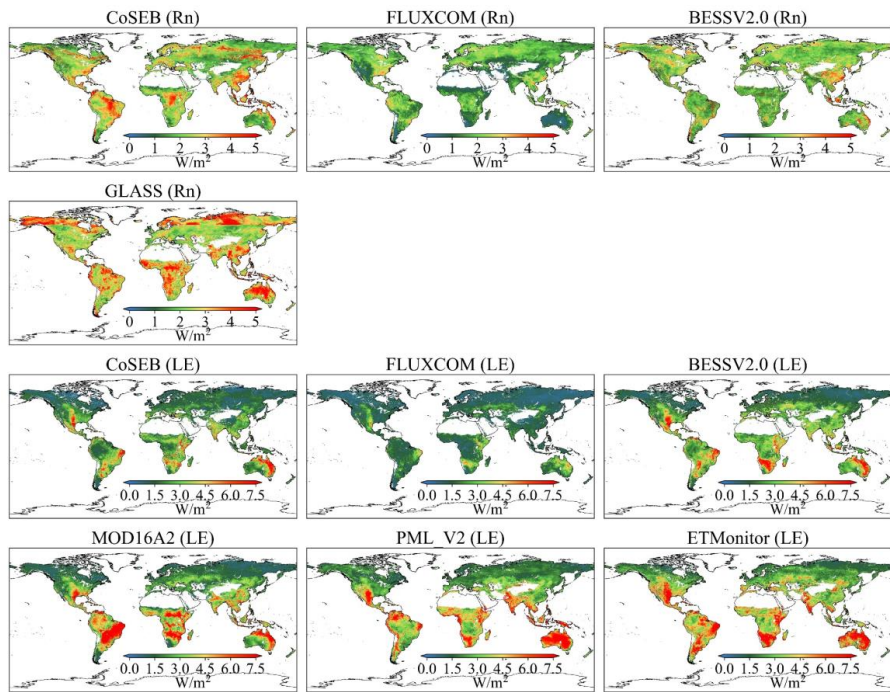


**Fig. 15** Spatial distribution of interannual variability (standard deviation) of downward shortwave radiation ( $SW_{IN}$ , the first row), downward longwave radiation ( $LW_{IN}$ , the second row) and upward longwave radiation ( $LW_{OUT}$ , the third row) from 2001 to 2018 by the CoSEB-based datasets, GLASS and BESS-Rad.

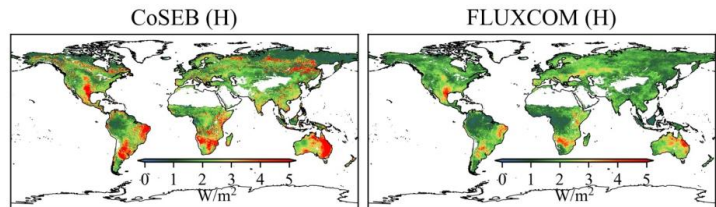
Figs. 15, 16 and 17 show the spatial patterns (excluding Greenland, Antarctic continent, deserts, water bodies and permanent snow) of interannual variability of  $SW_{IN}$ ,  $LW_{IN}$  and  $LW_{OUT}$ ,  $R_n$  and  $LE$ , as well as  $H$  from 2001 to 2018, respectively, derived from the CoSEB-based datasets and mainstream products/datasets. In general, the estimates from the CoSEB-based datasets displayed similar interannual variability in space with those from the mainstream products/datasets. Specially, the estimates of  $SW_{IN}$  from the CoSEB-based datasets, BESS-Rad, and GLASS exhibited a significant interannual variability mainly in northeastern Australia, eastern South America, Southeast China, and Southwest North America. The interannual variability of  $LW_{IN}$  and  $LW_{OUT}$  by the CoSEB-based datasets and GLASS displayed high values primarily at middle-to-high latitudes of the North Hemisphere and parts of Africa and Australia. The interannual variability of  $R_n$  observed by the CoSEB-based datasets was generally lower than that of GLASS, but higher than that of BESSV2.0 and FLUXCOM. The CoSEB-based datasets missed the strong interannual variability of  $LE$  as observed in MOD16A2, PML\_V2 and ETMonitor in parts of Africa, Australia and eastern South



535 America. Furthermore, FLUXCOM exhibited the weakest interannual variability of LE  
536 in almost all regions. The interannual variability of H derived from the CoSEB-based  
537 datasets was higher than those from FLUXCOM, with stronger interannual variabilities  
538 mainly observed in parts of eastern South America, southern Africa, and northeastern  
539 Australia.



540  
541 **Fig. 16** Spatial distribution of interannual variability (standard deviation) of net radiation (Rn,  
542 the first and second rows) and latent heat flux (LE, the third and fourth row) from 2001 to  
543 2018 by the CoSEB-based datasets, FLUXCOM, BESSV2.0, MOD16A2, PML\_V2,  
544 ETMonitor and GLASS.



545  
546 **Fig. 17** Spatial distribution of interannual variability (standard deviation) of sensible heat flux  
547 (H) from 2001 to 2018 by the CoSEB-based datasets and FLUXCOM.





## 548    **5 Discussion**

549            Accurately monitoring the spatial and temporal variations of global land surface  
 550    radiation and heat fluxes is crucial for quantifying the exchange of radiation, heat and  
 551    water between the land and atmosphere under global climate change (Chen et al., 2020;  
 552    Du et al., 2024; Kim et al., 2023; Liang et al., 2006; Wang et al., 2020). However,  
 553    although numerous global RS-based products/datasets of land surface radiation and  
 554    heat fluxes have been developed using physical and/or statistical methods, they  
 555    typically provide either merely a single flux or multiple fluxes (see Table 1) that are  
 556    estimated separately from uncoordinated models (Huang et al., 2024; Jung et al., 2019;  
 557    Sun et al., 2023; Tang et al., 2019), leading to noticeable radiation imbalance and/or  
 558    heat imbalance when these products are combined for practical applications. To address  
 559    these limitations, we generated high-accuracy global datasets of land surface radiation  
 560    and heat fluxes from 2000 to 2020 that adhere to both radiation and heat conservation  
 561    laws, using our proposed CoSEB model (Wang et al., 2025).

562            Our CoSEB model, integrating underlying physical principles of training datasets  
 563    into machine learning technique to effectively learn the interrelations among multiple  
 564    targeted outputs, was originally designed for coordinating estimates of global land  
 565    surface energy balance components ( $R_n$ ,  $LE$ ,  $H$  and  $G$ ) to satisfy the energy  
 566    conservation (Wang et al., 2025). Inspired by the idea of constructing the CoSEB model,  
 567    we further incorporated land surface radiation fluxes into our model to simultaneously  
 568    consider the physical constraints of both surface radiation and heat conservation  
 569    principles, by renewing the CoSEB using remote sensing products, reanalysis datasets,  
 570    as well as in situ observations of  $SW_{IN}$ ,  $SW_{OUT}$ ,  $LW_{IN}$ ,  $LW_{OUT}$ ,  $R_n$ ,  $LE$ ,  $H$  and  $G$ . To  
 571    comprehensively account for the main factors influencing surface radiation and heat  
 572    fluxes (Amani & Shafizadeh-Moghadam, 2023; Mohan et al., 2020; Wang et al., 2021),  
 573    the renewed CoSEB model utilized 19 easily accessible parameters/variables from  
 574    ERA5-Land reanalysis datasets, GLASS products, MODIS products, GMTED2010 and  
 575    NOAA/GML as input, which were readily available to generate datasets of global land



576 surface radiation and heat fluxes in a practical and operational manner.

577 The main advantages of our CoSEB-based datasets of land surface radiation and  
 578 heat fluxes lie in that [1] they are the first RS-based global datasets that satisfy both  
 579 surface radiation balance (  $SW_{IN} - SW_{OUT} + LW_{IN} - LW_{OUT} = Rn$  ) and heat balance  
 580 (  $LE + H + G = Rn$  ) among the eight fluxes, as demonstrated by both the RIR and EIR  
 581 of 0, [2] the radiation and heat fluxes are characterized by high accuracies when  
 582 validated against in situ measurements at 134 “homogeneous” sites (see the first  
 583 paragraph in Section 4.2), where (1) the RMSEs for daily estimates of  $SW_{IN}$ ,  $SW_{OUT}$ ,  
 584  $LW_{IN}$ ,  $LW_{OUT}$ ,  $Rn$ ,  $LE$ ,  $H$  and  $G$  from the CoSEB-based datasets were 28.51 W/m<sup>2</sup>, 10.39  
 585 W/m<sup>2</sup>, 14.29 W/m<sup>2</sup>, 10.62 W/m<sup>2</sup>, 22.40 W/m<sup>2</sup>, 24.38 W/m<sup>2</sup>, 22.67 W/m<sup>2</sup> and 6.77 W/m<sup>2</sup>,  
 586 respectively, as well as for 8-day estimates were 12.81 W/m<sup>2</sup>, 7.08 W/m<sup>2</sup>, 9.22 W/m<sup>2</sup>,  
 587 8.34 W/m<sup>2</sup>, 13.38 W/m<sup>2</sup>, 19.99 W/m<sup>2</sup>, 17.44 W/m<sup>2</sup> and 4.25 W/m<sup>2</sup>, respectively, (2) the  
 588 CoSEB-based datasets, in comparison to the mainstream products/datasets (i.e. GLASS,  
 589 BESS-Rad, FLUXCOM, BESSV2.0, MOD16A2, PML\_V2 and ETMonitor), better  
 590 agreed with the in situ observations at 134 EC sites, showing the RMSE reductions  
 591 ranging from 4.35 W/m<sup>2</sup> to 11.46 W/m<sup>2</sup> for  $SW_{IN}$ ,  $LW_{IN}$ ,  $LW_{OUT}$ ,  $Rn$  and  $LE$  at daily  
 592 scale, and 4.62 W/m<sup>2</sup> to 14.64 W/m<sup>2</sup> for  $SW_{IN}$ ,  $LW_{IN}$ ,  $LW_{OUT}$ ,  $Rn$ ,  $LE$  and  $H$  at 8-day  
 593 scale.

594 Our developed datasets could be potentially applied in many fields, including but  
 595 not limited to (1) exploring the spatial-temporal patterns of global land surface radiation  
 596 and heat flux (es) and their driving mechanisms over the past decades under global  
 597 change (e.g., rising CO<sub>2</sub> concentration, greening land surface and increasing air  
 598 temperature), (2) investigating the variability of land surface radiation and heat fluxes  
 599 caused by extreme events and human activities, e.g. afforestation or deforestation,  
 600 wildfire, air pollution, weather extremes and urbanization, (3) assessing the resources  
 601 of solar energy, geothermal energy, surface and ground water at regional and global  
 602 scales, (4) monitoring natural hazards, e.g. drought in agriculture and forestry.

603 The uncertainties of our datasets are relevant to (1) the data preprocessing, and (2)



the application of the CoSEB at different spatial scales. Specifically, the daily average of surface radiation and heat fluxes for each day was obtained for analysis from good-quality half-hourly observations when the fraction of these good-quality half-hourly observations was greater than 80% in a day, due to the lack of consensus on the method for aggregating gapped half-hourly observations to daily data (Tang et al., 2024a; Yao et al., 2017; Zheng et al., 2022). Likewise, since there was no agreement on how to correct for the energy imbalance of turbulent heat fluxes, we adopted the most widely applied Bowen ratio method to enforce energy closure between  $R_n - G$  and  $LE + H$  (Castelli et al., 2018; Twine et al., 2000; Zhang et al., 2021). These data preprocessing had an effect on the construction of the renewed CoSEB model, which may further affect the global datasets. Moreover, the renewed CoSEB model was constructed at the spatial scale of 500 m to match the footprints of the in situ EC observations, but applied at the spatial resolution of  $0.05^\circ$  to generate global datasets, mainly limited by the computing and storage capabilities in our personal computers. However, the CoSEB-based datasets have also been validated and inter-compared at 134 EC sites to demonstrate that the difference in spatial scale would not much affect the performance of the datasets. Despite these uncertainties, it is worth emphasizing that our work was the first attempt to innovatively develop energy-conservation datasets of global land surface radiation and heat fluxes with high accuracies.

## 6 Data availability

The energy-conservation datasets of global land surface radiation and heat fluxes generated by the CoSEB model with spatial-temporal resolutions of daily and  $0.05^\circ$  from Feb.26, 2000 to Dec.31, 2020 are freely available through the National Tibetan Plateau Data Center at <https://doi.org/10.11888/Terre.tpd.c.302559> (Tang et al., 2025a) and through the Science Data Bank (ScienceDB) at <https://doi.org/10.57760/sciencedb.27228> (Tang et al., 2025b).





## 630 7 Summary and Conclusion

631 This study for the first time developed energy-conservation datasets of global land  
 632 surface radiation and heat fluxes using our CoSEB model renewed based on GLASS  
 633 and MODIS products, ERA5-Land reanalysis datasets, topographic data, CO<sub>2</sub>  
 634 concentration data, and observations at 258 EC sites worldwide from the FLUXNET,  
 635 AmeriFlux, EuroFlux, OzFlux, ChinaFLUX and TPDC.

636 The CoSEB-based datasets of land surface radiation and heat fluxes are the first  
 637 RS-based global datasets that satisfy both surface radiation balance  
 638 ( $SW_{IN} - SW_{OUT} + LW_{IN} - LW_{OUT} = R_n$ ) and heat balance ( $LE + H + G = R_n$ ) among the  
 639 eight fluxes. Meanwhile, the CoSEB-based datasets outperformed the mainstream  
 640 products/datasets in accuracy. Specifically, at 134 EC sites, the RMSEs for daily  
 641 estimates of  $SW_{IN}$ ,  $SW_{OUT}$ ,  $LW_{IN}$ ,  $LW_{OUT}$ ,  $R_n$ ,  $LE$ ,  $H$  and  $G$  from the CoSEB-based datasets  
 642 were 28.51 W/m<sup>2</sup>, 10.39 W/m<sup>2</sup>, 14.29 W/m<sup>2</sup>, 10.62 W/m<sup>2</sup>, 22.40 W/m<sup>2</sup>, 24.38 W/m<sup>2</sup>,  
 643 22.67 W/m<sup>2</sup> and 6.77 W/m<sup>2</sup>, respectively, as well as for 8-day estimates were 12.81  
 644 W/m<sup>2</sup>, 7.08 W/m<sup>2</sup>, 9.22 W/m<sup>2</sup>, 8.34 W/m<sup>2</sup>, 13.38 W/m<sup>2</sup>, 19.99 W/m<sup>2</sup>, 17.44 W/m<sup>2</sup> and  
 645 4.25 W/m<sup>2</sup>, respectively. Moreover, the estimates from the CoSEB-based datasets in  
 646 comparison to those from the mainstream products/datasets reduced the RMSE by 4.35  
 647 W/m<sup>2</sup> to 11.46 W/m<sup>2</sup> and increased the  $R^2$  by 0.04 to 0.3 for  $SW_{IN}$ ,  $LW_{IN}$ ,  $LW_{OUT}$ ,  $R_n$   
 648 and  $LE$  at daily scale, and reduced the RMSE by 4.62 W/m<sup>2</sup> to 14.64 W/m<sup>2</sup> and  
 649 increased the  $R^2$  by 0.04 to 0.41 for  $SW_{IN}$ ,  $LW_{IN}$ ,  $LW_{OUT}$ ,  $R_n$ ,  $LE$  and  $H$  at 8-day scale,  
 650 when these estimates were validated against in situ observations at 134 EC sites.  
 651 Furthermore, the CoSEB-based datasets effectively captured the spatial-temporal  
 652 variability of global land surface radiation and heat fluxes, aligning well with those  
 653 from the mainstream products.

654 Our developed datasets hold significant potential for application across diverse  
 655 fields such as agriculture, forestry, hydrology, meteorology, ecology, and environmental  
 656 science. They can facilitate comprehensive studies on the variability, impacts, responses,  
 657 adaptation strategies, and mitigation measures of global and regional land surface



658 radiation and heat fluxes under the influences of climate change and human activities.  
659 These datasets will provide valuable insights and data support for scientific research,  
660 policy-making, and environmental management, advancing global solutions to address  
661 climate change.

#### 662 **Author contribution**

663 JW: Writing – original draft, Visualization, Software, Formal analysis, Data  
664 curation. RT: Writing – original draft, Validation, Supervision, Methodology, Funding  
665 acquisition, Formal analysis, Conceptualization. ML: Writing – review & editing,  
666 Validation. ZL: Writing – review & editing.

#### 667 **Competing interests**

668 The authors declare that they have no conflict of interest.

#### 669 **Acknowledgment**

670 We thank the work from the AmeriFlux, FLUXNET, EuroFlux, OzFlux,  
671 ChinaFLUX, the National Tibetan Plateau/Third Pole Environment Data Center and  
672 SURFRAD for providing in situ measurements. We would also like to thank Dr. Martin  
673 Jung and Dr. Ulrich Weber for providing the FLUXCOM Bowen ratio-corrected  
674 products. This work is supported by the National Natural Science Foundation of China  
675 [42271378], and the Strategic Priority Research Program of the Chinese Academy of  
676 Sciences (Grant No. XDB0740202).  
677



## 678 References

- 679 Amani, S. and Shafizadeh-Moghadam, H.: A review of machine learning models and  
 680 influential factors for estimating evapotranspiration using remote sensing and  
 681 ground-based data, *Agric. Water Manage.*, 284, 108324.  
 682 10.1016/j.agwat.2023.108324, 2023.
- 683 Berbery, E. H., Mitchell, K. E., Benjamin, S., Smirnova, T., Ritchie, H., Hogue, R. and  
 684 Radeva, E.: Assessment of land - surface energy budgets from regional and  
 685 global models, *J. Geophys. Res.-Atmos.*, 104, 19329-19348.  
 686 10.1029/1999jd900128, 1999.
- 687 Betts, A. K., Ball, J. H., Beljaars, A. C. M., Miller, M. J. and Viterbo, P. A.: The land  
 688 surface - atmosphere interaction: A review based on observational and global  
 689 modeling perspectives, *J. Geophys. Res.-Atmos.*, 101, 7209-7225.  
 690 10.1029/95jd02135, 1996.
- 691 Castelli, M., Anderson, M. C., Yang, Y., Wohlfahrt, G., Bertoldi, G., Niedrist, G.,  
 692 Hammerle, A., Zhao, P., Zebisch, M. and Notarnicola, C.: Two-source energy  
 693 balance modeling of evapotranspiration in Alpine grasslands, *Remote Sens.*  
 694 *Environ.*, 209, 327-342. 10.1016/j.rse.2018.02.062, 2018.
- 695 Chen, J., He, T., Jiang, B. and Liang, S.: Estimation of all-sky all-wave daily net  
 696 radiation at high latitudes from MODIS data, *Remote Sens. Environ.*, 245,  
 697 111842. 10.1016/j.rse.2020.111842, 2020.
- 698 de Wit, A. J. W., Boogaard, H. L. and van Diepen, C. A.: Spatial resolution of  
 699 precipitation and radiation: The effect on regional crop yield forecasts, *Agric.*  
 700 *For. Meteorol.*, 135, 156-168. 10.1016/j.agrformet.2005.11.012, 2005.
- 701 Du, Y., Wang, T., Zhou, Y., Letu, H., Li, D. and Xian, Y.: Towards user-friendly all-sky  
 702 surface longwave downward radiation from space: General scheme and product,  
 703 *Bull. Amer. Meteorol. Soc.*, 105, E1303–E1319. 10.1175/bams-d-23-0126.1,  
 704 2024.
- 705 Ersi, C., Sudu, B., Song, Z., Bao, Y., Wei, S., Zhang, J., Tong, Z., Liu, X., Le, W. and  
 706 Rina, S.: The potential of NIRvP in estimating evapotranspiration, *Remote Sens.*  
 707 *Environ.*, 315, 114405. 10.1016/j.rse.2024.114405, 2024.
- 708 Huang, J., Yu, H., Guan, X., Wang, G. and Guo, R.: Accelerated dryland expansion  
 709 under climate change, *Nat. Clim. Chang.*, 6, 166-171. 10.1038/nclimate2837,  
 710 2015.
- 711 Huang, L., Luo, Y., Chen, J. M., Tang, Q., Steenhuis, T., Cheng, W. and Shi, W.:  
 712 Satellite-based near-real-time global daily terrestrial evapotranspiration  
 713 estimates, *Earth Syst. Sci. Data*, 16, 3993-4019. 10.5194/essd-16-3993-2024,  
 714 2024.
- 715 Jia, B., Xie, Z., Dai, A., Shi, C. and Chen, F.: Evaluation of satellite and reanalysis  
 716 products of downward surface solar radiation over East Asia: Spatial and  
 717 seasonal variations, *J. Geophys. Res.-Atmos.*, 118, 3431-3446.  
 718 10.1002/jgrd.50353, 2013.



- 719 Jiang, B., Zhang, Y., Liang, S., Wohlfahrt, G., Arain, A., Cescatti, A., Georgiadis, T., Jia,  
 720 K., Kiely, G., Lund, M., Montagnani, L., Magliulo, V., Ortiz, P. S., Oechel, W.,  
 721 Vaccari, F. P., Yao, Y. and Zhang, X.: Empirical estimation of daytime net  
 722 radiation from shortwave radiation and ancillary information, *Agric. For.*  
 723 *Meteorol.*, 211-212, 23-36. 10.1016/j.agrformet.2015.05.003, 2015.
- 724 Jiao, B., Su, Y., Li, Q., Manara, V. and Wild, M.: An integrated and homogenized global  
 725 surface solar radiation dataset and its reconstruction based on a convolutional  
 726 neural network approach, *Earth Syst. Sci. Data*, 15, 4519-4535. 10.5194/essd-  
 727 15-4519-2023, 2023.
- 728 Jung, M., Koirala, S., Weber, U., Ichii, K., Gans, F., Camps-Valls, G., Papale, D.,  
 729 Schwalm, C., Tramontana, G. and Reichstein, M.: The FLUXCOM ensemble of  
 730 global land-atmosphere energy fluxes, *Sci. Data*, 6, 74. 10.1038/s41597-019-  
 731 0076-8, 2019.
- 732 Kim, Y., Park, H., Kimball, J. S., Colliander, A. and McCabe, M. F.: Global estimates  
 733 of daily evapotranspiration using SMAP surface and root-zone soil moisture,  
 734 *Remote Sens. Environ.*, 298, 113803. 10.1016/j.rse.2023.113803, 2023.
- 735 Li, B., Ryu, Y., Jiang, C., Dechant, B., Liu, J., Yan, Y. and Li, X.: BESSv2.0: A satellite-  
 736 based and coupled-process model for quantifying long-term global land-  
 737 atmosphere fluxes, *Remote Sens. Environ.*, 295, 113696.  
 738 10.1016/j.rse.2023.113696, 2023.
- 739 Liang, S., Wang, D., He, T. and Yu, Y.: Remote sensing of earth's energy budget:  
 740 synthesis and review, *Int. J. Digit. Earth*, 12, 737-780.  
 741 10.1080/17538947.2019.1597189, 2019.
- 742 Liang, S., Zheng, T., Liu, R., Fang, H., Tsay, S. C. and Running, S.: Estimation of  
 743 incident photosynthetically active radiation from Moderate Resolution Imaging  
 744 Spectrometer data, *J. Geophys. Res.-Atmos.*, 111. 10.1029/2005jd006730, 2006.
- 745 Liu, S., Xu, Z., Song, L., Zhao, Q., Ge, Y., Xu, T., Ma, Y., Zhu, Z., Jia, Z. and Zhang,  
 746 F.: Upscaling evapotranspiration measurements from multi-site to the satellite  
 747 pixel scale over heterogeneous land surfaces, *Agric. For. Meteorol.*, 230, 97-113.  
 748 10.1016/j.agrformet.2016.04.008, 2016.
- 749 Martens, B., Miralles, D. G., Lievens, H., van der Schalie, R., de Jeu, R. A. M.,  
 750 Fernández-Prieto, D., Beck, H. E., Dorigo, W. A. and Verhoest, N. E. C.:  
 751 GLEAM v3: satellite-based land evaporation and root-zone soil moisture,  
 752 *Geosci. Model Dev.*, 10, 1903-1925. 10.5194/gmd-10-1903-2017, 2017.
- 753 Mohan, M. M. P., Kanchirapuzha, R. and Varma, M. R. R.: Review of approaches for  
 754 the estimation of sensible heat flux in remote sensing-based evapotranspiration  
 755 models, *J. Appl. Remote Sens.*, 14, 041501-041501. 10.1117/1.Jrs.14.041501,  
 756 2020.
- 757 Mu, Q., Zhao, M. and Running, S. W.: Improvements to a MODIS global terrestrial  
 758 evapotranspiration algorithm, *Remote Sens. Environ.*, 115, 1781-1800.  
 759 10.1016/j.rse.2011.02.019, 2011.
- 760 Mueller, R. W., Matsoukas, C., Gratzki, A., Behr, H. D. and Hollmann, R.: The CM-



- 761 SAF operational scheme for the satellite based retrieval of solar surface  
 762 irradiance — A LUT based eigenvector hybrid approach, *Remote Sens. Environ.*,  
 763 113, 1012-1024. 10.1016/j.rse.2009.01.012, 2009.
- 764 Muñoz-Sabater, J., Dutra, E., Agustí-Panareda, A., Albergel, C., Arduini, G., Balsamo,  
 765 G., Boussetta, S., Choulga, M., Harrigan, S., Hersbach, H., Martens, B.,  
 766 Miralles, D. G., Piles, M., Rodríguez-Fernández, N. J., Zsoter, E., Buontempo,  
 767 C. and Thépaut, J.-N.: ERA5-Land: a state-of-the-art global reanalysis dataset  
 768 for land applications, *Earth Syst. Sci. Data*, 13, 4349-4383. 10.5194/essd-13-  
 769 4349-2021, 2021.
- 770 Nemani, R. R., Keeling, C. D., Hashimoto, H., Jolly, W. M., Piper, S. C., Tucker, C. J.,  
 771 Myneni, R. B. and Running, S. W.: Climate-driven increases in global terrestrial  
 772 net primary production from 1982 to 1999, *Science*, 300, 1560-1563.  
 773 10.1126/science.1082750, 2003.
- 774 Rios, G. and Ramamurthy, P.: A novel model to estimate sensible heat fluxes in urban  
 775 areas using satellite-derived data, *Remote Sens. Environ.*, 270, 112880.  
 776 10.1016/j.rse.2021.112880, 2022.
- 777 Ryu, Y., Jiang, C., Kobayashi, H. and Detto, M.: MODIS-derived global land products  
 778 of shortwave radiation and diffuse and total photosynthetically active radiation  
 779 at 5 km resolution from 2000, *Remote Sens. Environ.*, 204, 812-825.  
 780 10.1016/j.rse.2017.09.021, 2018.
- 781 Salazar-Martínez, D., Holwerda, F., Holmes, T. R. H., Yépez, E. A., Hain, C. R.,  
 782 Alvarado-Barrientos, S., Ángeles-Pérez, G., Arredondo-Moreno, T., Delgado-  
 783 Balbuena, J., Figueroa-Espinoza, B., Garatuza-Payán, J., González del Castillo,  
 784 E., Rodríguez, J. C., Rojas-Robles, N. E., Uuh-Sonda, J. M. and Vivoni, E. R.:  
 785 Evaluation of remote sensing-based evapotranspiration products at low-latitude  
 786 eddy covariance sites, *J. Hydrol.*, 610, 127786. 10.1016/j.jhydrol.2022.127786,  
 787 2022.
- 788 Sellers, P. J., Dickinson, R. E., Randall, D. A., Betts, A. K., Hall, F. G., Berry, J. A.,  
 789 Collatz, G. J., Denning, A. S., Mooney, H. A., Nobre, C. A., Sato, N., Field, C.  
 790 B. and Henderson-Sellers, A.: Modeling the Exchanges of Energy, Water, and  
 791 Carbon Between Continents and the Atmosphere, *Science*, 275, 502-509.  
 792 10.1126/science.275.5299.502, 1997.
- 793 Sun, S., Bi, Z., Xiao, J., Liu, Y., Sun, G., Ju, W., Liu, C., Mu, M., Li, J., Zhou, Y., Li,  
 794 X., Liu, Y. and Chen, H.: A global 5 km monthly potential evapotranspiration  
 795 dataset (1982–2015) estimated by the Shuttleworth–Wallace model, *Earth Syst.*  
 796 *Sci. Data*, 15, 4849-4876. 10.5194/essd-15-4849-2023, 2023.
- 797 Tang, R., Peng, Z., Liu, M., Li, Z.-L., Jiang, Y., Hu, Y., Huang, L., Wang, Y., Wang, J.,  
 798 Jia, L., Zheng, C., Zhang, Y., Zhang, K., Yao, Y., Chen, X., Xiong, Y., Zeng, Z.  
 799 and Fisher, J. B.: Spatial-temporal patterns of land surface evapotranspiration  
 800 from global products, *Remote Sens. Environ.*, 304, 114066.  
 801 10.1016/j.rse.2024.114066, 2024a.
- 802 Tang, R., Wang, J., Liu, M. and Li, Z.-L.: Energy-conservation datasets of global land



- 803 surface radiation and heat fluxes from 2000-2020 generated by CoSEB,  
 804 National Tibetan Plateau / Third Pole Environment Data Center. [data set],  
 805 <https://doi.org/10.11888/Terre.tpdc.302559>, 2025a.
- 806 Tang, R., Wang, J., Liu, M. and Li, Z.-L.: Energy-conservation datasets of global land  
 807 surface radiation and heat fluxes from 2000-2020 generated by CoSEB, Science  
 808 Data Bank: Science Data Bank. [data set],  
 809 <https://doi.org/10.57760/sciencedb.27228>, 2025b.
- 810 Tang, W., He, J., Qi, J. and Yang, K.: A dense station-based, long-term and high-  
 811 accuracy dataset of daily surface solar radiation in China, Earth Syst. Sci. Data,  
 812 15, 4537-4551. 10.5194/essd-15-4537-2023, 2023.
- 813 Tang, W., He, J., Shao, C., Song, J., Yuan, Z. and Yan, B.: Constructing a long-term  
 814 global dataset of direct and diffuse radiation (10 km, 3 h, 1983–2018) separating  
 815 from the satellite-based estimates of global radiation, Remote Sens. Environ.,  
 816 311, 114292. 10.1016/j.rse.2024.114292, 2024b.
- 817 Tang, W., Yang, K., Qin, J., Li, X. and Niu, X.: A 16-year dataset (2000–2015) of high-  
 818 resolution (3 h, 10 km) global surface solar radiation, Earth Syst. Sci. Data, 11,  
 819 1905-1915. 10.5194/essd-11-1905-2019, 2019.
- 820 Twine, T. E., Kustas, W. P., Norman, J. M., Cook, D. R., Houser, P. R., Meyers, T. P.,  
 821 Prueger, J. H., Starks, P. J. and Wesely, M. L.: Correcting eddy-covariance flux  
 822 underestimates over a grassland, Agric. For. Meteorol., 103, 279-300.  
 823 10.1016/S0168-1923(00)00123-4, 2000.
- 824 van der Tol, C.: Validation of remote sensing of bare soil ground heat flux, Remote Sens.  
 825 Environ., 121, 275-286. 10.1016/j.rse.2012.02.009, 2012.
- 826 Wang, D., Liang, S., He, T. and Shi, Q.: Estimation of Daily Surface Shortwave Net  
 827 Radiation From the Combined MODIS Data, IEEE Trans. Geosci. Remote  
 828 Sensing, 53, 5519-5529. 10.1109/tgrs.2015.2424716, 2015.
- 829 Wang, D., Liang, S., Li, R. and Jia, A.: A synergic study on estimating surface  
 830 downward shortwave radiation from satellite data, Remote Sens. Environ., 264,  
 831 112639. 10.1016/j.rse.2021.112639, 2021.
- 832 Wang, J., Tang, R., Liu, M., Jiang, Y., Huang, L. and Li, Z.-L.: Coordinated estimates  
 833 of 4-day 500 m global land surface energy balance components, Remote Sens.  
 834 Environ., 326, 114795. 10.1016/j.rse.2025.114795, 2025.
- 835 Wang, K. C., Dickinson, R. E., Wild, M. and Liang, S.: Atmospheric impacts on climatic  
 836 variability of surface incident solar radiation, Atmos. Chem. Phys., 12, 9581-  
 837 9592. 10.5194/acp-12-9581-2012, 2012.
- 838 Wang, T., Shi, J., Ma, Y., Letu, H. and Li, X.: All-sky longwave downward radiation  
 839 from satellite measurements: General parameterizations based on LST, column  
 840 water vapor and cloud top temperature, ISPRS-J. Photogramm. Remote Sens.,  
 841 161, 52-60. 10.1016/j.isprsjprs.2020.01.011, 2020.
- 842 Wild, M.: Global dimming and brightening: A review, J. Geophys. Res.-Atmos., 114,  
 843 10.1029/2008jd011470, 2009.
- 844 Wild, M., Folini, D., Schär, C., Loeb, N., Dutton, E. G. and König-Langlo, G.: The



- 845 global energy balance from a surface perspective, *Clim. Dyn.*, 40, 3107-3134.
- 846 10.1007/s00382-012-1569-8, 2012.
- 847 Wild, M. and Liepert, B.: The Earth radiation balance as driver of the global
- 848 hydrological cycle, *Environ. Res. Lett.*, 0, 025203. 10.1088/1748-
- 849 9326/5/2/025003, 2010.
- 850 Xia, X. A., Wang, P. C., Chen, H. B. and Liang, F.: Analysis of downwelling surface
- 851 solar radiation in China from National Centers for Environmental Prediction
- 852 reanalysis, satellite estimates, and surface observations, *J. Geophys. Res.-*
- 853 *Atmos.*, 111. 10.1029/2005jd006405, 2006.
- 854 Xu, J., Liang, S. and Jiang, B.: A global long-term (1981–2019) daily land surface
- 855 radiation budget product from AVHRR satellite data using a residual
- 856 convolutional neural network, *Earth Syst. Sci. Data*, 14, 2315-2341.
- 857 10.5194/essd-14-2315-2022, 2022a.
- 858 Xu, J., Liang, S., Ma, H. and He, T.: Generating 5 km resolution 1981–2018 daily global
- 859 land surface longwave radiation products from AVHRR shortwave and
- 860 longwave observations using densely connected convolutional neural networks,
- 861 *Remote Sens. Environ.*, 280, 113223. 10.1016/j.rse.2022.113223, 2022b.
- 862 Yao, Y., Liang, S., Li, X., Chen, J., Liu, S., Jia, K., Zhang, X., Xiao, Z., Fisher, J. B.,
- 863 Mu, Q., Pan, M., Liu, M., Cheng, J., Jiang, B., Xie, X., Grünwald, T., Bernhofer,
- 864 C. and Rouspard, O.: Improving global terrestrial evapotranspiration estimation
- 865 using support vector machine by integrating three process-based algorithms,
- 866 *Agric. For. Meteorol.*, 242, 55-74. 10.1016/j.agrformet.2017.04.011, 2017.
- 867 Yu, L., Qiu, G. Y., Yan, C., Zhao, W., Zou, Z., Ding, J., Qin, L. and Xiong, Y.: A global
- 868 terrestrial evapotranspiration product based on the three-temperature model
- 869 with fewer input parameters and no calibration requirement, *Earth Syst. Sci.*
- 870 *Data*, 14, 3673-3693. 10.5194/essd-14-3673-2022, 2022.
- 871 Zhang, C., Long, D., Zhang, Y., Anderson, M. C., Kustas, W. P. and Yang, Y.: A decadal
- 872 (2008–2017) daily evapotranspiration data set of 1 km spatial resolution and
- 873 spatial completeness across the North China Plain using TSEB and data fusion,
- 874 *Remote Sens. Environ.*, 262, 112519. 10.1016/j.rse.2021.112519, 2021.
- 875 Zhang, J., Zhao, L., Deng, S., Xu, W. and Zhang, Y.: A critical review of the models
- 876 used to estimate solar radiation, *Renew. Sust. Energ. Rev.*, 70, 314-329.
- 877 10.1016/j.rser.2016.11.124, 2017.
- 878 Zhang, K., Kimball, J. S., Nemani, R. R. and Running, S. W.: A continuous satellite -
- 879 derived global record of land surface evapotranspiration from 1983 to 2006,
- 880 *Water Resour. Res.*, 46, W09522. 10.1029/2009wr008800, 2010.
- 881 Zhang, X., Liang, S., Zhou, G., Wu, H. and Zhao, X.: Generating Global LAnd Surface
- 882 Satellite incident shortwave radiation and photosynthetically active radiation
- 883 products from multiple satellite data, *Remote Sens. Environ.*, 152, 318-332.
- 884 10.1016/j.rse.2014.07.003, 2014.
- 885 Zhang, Y., Kong, D., Gan, R., Chiew, F. H. S., McVicar, T. R., Zhang, Q. and Yang, Y.:
- 886 Coupled estimation of 500 m and 8-day resolution global evapotranspiration



887                   and gross primary production in 2002–2017, Remote Sens. Environ., 222, 165-  
888                   182. 10.1016/j.rse.2018.12.031, 2019.  
889           Zheng, C., Jia, L. and Hu, G.: Global land surface evapotranspiration monitoring by  
890           ETMonitor model driven by multi-source satellite earth observations, J. Hydrol.,  
891           613, 128444. 10.1016/j.jhydrol.2022.128444, 2022.  
892